Nano Research

ISSN 1998-0124 CN 11-5974/O4
https://doi.org/10.26599/NR.2026.94908832

Research Article

A multi-enzyme mimetic nanozyme sensitizes esophageal cancer to CDK4/6 inhibition via oxidative stress

Ling Lan[1,2,§], Jiwen Fan[3,§], Yang Li[4,§], Zihan Li[3], Zhu Yuan[1], Imran Shakir[5], Binwu Ying[3], Limei Luo[3](✉), Yi Li[3](✉), Xuping Sun[6,7], Jin Zhou[2](✉)

[1] Department of Biotherapy, Cancer Center and State Key Laboratory of Biotherapy, West China Hospital, Sichuan University, Chengdu 610041, China

[2] Division of Liver Surgery, Department of General Surgery, West China Hospital, Sichuan University, Chengdu 610041, China

[3] Department of Laboratory Medicine/Clinical Laboratory Medicine Research Center, West China Hospital, Sichuan University, Chengdu 610041, China

[4] Division of Gastrointestinal Surgery Ward, Department of General Surgery, West China Hospital, Sichuan University, Chengdu 610041, China

[5] Department of Physics, Faculty of Science, Islamic University of Madinah, Madinah 42351, Saudi Arabia

[6] Center for High Altitude Medicine, West China Hospital, Sichuan University, Chengdu 610041, China

[7] College of Chemistry, Chemical Engineering and Materials Science, Shandong Normal University, Jinan 250014, China

[§] Ling Lan, Jiwen Fan, and Yang Li contributed equally to this work.

Nano Res., **Just Accepted Manuscript** • https://doi.org/10.26599/NR.2026.94908832

https://www.sciopen.com/journal/1998-0124 on May. 11, 2026

A multi-enzyme mimetic nanozyme sensitizes esophageal cancer to CDK4/6 inhibition via oxidative stress

Ling Lan[1], Jiwen Fan[1], Yang Li[1], Zihan Li[1], Zhu Yuan[1], Imran Shakir[2], Binwu Ying[1], Limei Luo[1], Yi Li[1], and Xuping Sun[1,3], and Jin Zhou[1]

1. Sichuan University, China
2. Islamic University of Madinah, Saudi Arabia
3. Shandong Normal University, China

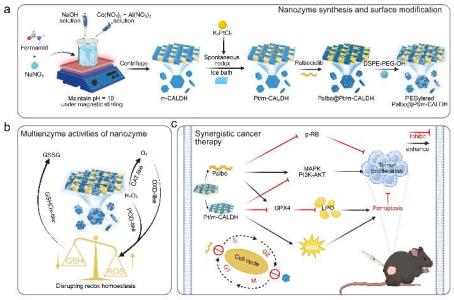

A multi-enzyme mimetic nanozyme–drug platform amplifies oxidative stress and disrupts redox homeostasis to sensitize tumors to CDK4/6 inhibition for enhanced cancer therapy.

Nano Research

ISSN 1998-0124 CN 11-5974/O4
https://doi.org/10.26599/NR.2026.94908832

Research Article

A multi-enzyme mimetic nanozyme sensitizes esophageal cancer to CDK4/6 inhibition via oxidative stress

Ling Lan[1,2,§], Jiwen Fan[3,§], Yang Li[4,§], Zihan Li[3], Zhu Yuan[1], Imran Shakir[5], Binwu Ying[3], Limei Luo[3](✉), Yi Li[3](✉), Xuping Sun[6,7], and Jin Zhou[2](✉)

[1] *Department of Biotherapy, Cancer Center and State Key Laboratory of Biotherapy, West China Hospital, Sichuan University, Chengdu 610041, China*
[2] *Division of Liver Surgery, Department of General Surgery, West China Hospital, Sichuan University, Chengdu 610041, China*
[3] *Department of Laboratory Medicine/Clinical Laboratory Medicine Research Center, West China Hospital, Sichuan University, Chengdu 610041, China*
[4] *Division of Gastrointestinal Surgery Ward, Department of General Surgery, West China Hospital, Sichuan University, Chengdu 610041, China*
[5] *Department of Physics, Faculty of Science, Islamic University of Madinah, Madinah 42351, Saudi Arabia*
[6] *Center for High Altitude Medicine, West China Hospital, Sichuan University, Chengdu 610041, China*
[7] *College of Chemistry, Chemical Engineering and Materials Science, Shandong Normal University, Jinan 250014, China*
[§] *Ling Lan, Jiwen Fan, and Yang Li contributed equally to this work.*

Received: 13 March 2026 / **Revised:** 8 May 2026 / **Accepted:** 11 May 2026

ABSTRACT: **Esophageal squamous cell carcinoma (ESCC) exhibits frequent cell cycle pathway alterations, particularly hyperactivation of the Cyclin D1/Cyclin-dependent kinase 4 and 6 (CDK4/6) axis, but clinical trials of CDK4/6 inhibitor palbociclib in ESCC have not shown evidence of curative effect. In this work, we rationally engineered a Pt nanoparticle-decorated monolayer CoAl layered double hydroxide nanosheet to sensitize palbociclib and achieve synergistic antitumor efficacy in ESCC model. The nanosheet exhibits multienzyme-mimicking activities, including glutathione oxidase, catalase, oxidase, and peroxidase-like, which generate substantial reactive oxygen species (ROS) together with intracellular glutathione depletion. The elevated ROS levels effectively attenuate palbociclib-triggered adaptive responses, including compensatory activation of MAPK, PI3K-AKT-mTOR signaling pathways and the upregulation of glutathione peroxidase 4, thereby enhancing tumor suppression. Our work highlights nanozyme-mediated oxidative stress amplification as a promising strategy for sensitizing molecular-targeted therapies.**

KEYWORDS: **nanozyme, esophageal squamous cell carcinoma, synergistic cancer therapy, CDK4/6 inhibitor, molecular target**

1 Introduction

Esophageal cancer ranks as the seventh leading cause of cancer-related deaths worldwide, with esophageal squamous cell carcinoma (ESCC) representing the main subtype and accounting for nearly 90% of cases [1–3]. Although advances in systemic therapies, including immune checkpoint blockade combined with chemotherapy, have improved outcomes for certain patient populations, the prognosis of advanced ESCC remains unsatisfactory [4–6]. Increasing attention has been directed toward identifying molecular vulnerabilities that could be exploited for targeted therapeutic intervention [7, 8]. Among these, dysregulation of cell cycle control is one of the most pervasive oncogenic features in ESCC [9, 10].

Large-scale genomic analyses, including those from The Cancer Genome Atlas, have revealed that alterations affecting cell cycle regulatory networks occur in more than 90% of ESCC tumors [11–13]. Amplification of cyclin D1 (CCND1) and loss or mutation of the CDKN2A tumor suppressor gene are particularly common events, collectively resulting in persistent activation of the cyclin D1–cyclin-dependent kinase 4 and 6 (CDK4/6) axis [14, 15]. These findings provide a strong biological rationale for targeting CDK4/6 signaling in ESCC. Indeed, CDK4/6 inhibitors such as palbociclib, ribociclib, and abemaciclib have achieved notable clinical success in hormone receptor–positive breast cancer [16–18]. However, the therapeutic benefit of CDK4/6 inhibition in ESCC has been far less pronounced. A phase II clinical study evaluating palbociclib monotherapy in ESCC patients reported no objective responses [19], indicating that tumor cells may rapidly engage adaptive mechanisms that restrict the efficacy of CDK4/6 blockade.

Accumulating evidence suggests that oncogenic signaling networks can compensate for CDK4/6 inhibition and thereby diminish its antitumor activity [20–22]. In particular, the mitogen-activated protein kinase (MAPK) cascade and the phosphatidylinositol 3-kinase (PI3K)–protein kinase B (AKT) –mammalian target of rapamycin (mTOR) pathway are frequently activated in ESCC and play central roles in regulating cell proliferation, survival, and metabolic adaptation [23, 24]. These pathways have also been implicated in the control of CCND1 expression through multiple regulatory layers, including

Address correspondence to Limei Luo, luolimei@scu.edu.cn; Yi Li, liyi12@scu.edu.cn; Jin Zhou, zhoujin096@scu.edu.cn

transcriptional activation, enhanced mRNA translation, and stabilization of the cyclin D1 protein [25–27]. Such signaling plasticity suggests that modulation of the cellular signaling environment may represent an effective strategy to enhance tumor responsiveness to CDK4/6 inhibition.

Reactive oxygen species (ROS) are increasingly recognized as important modulators of oncogenic signaling pathways [28–30]. While moderate ROS levels can promote tumor progression by stimulating proliferative signaling, excessive oxidative stress disrupts redox homeostasis and can impair multiple survival pathways in cancer cells [31–33]. In this context, nanozymes, nanostructured materials capable of mimicking enzymatic catalytic activities, have emerged as promising tools for therapeutic redox regulation [34–36]. Recent advances in nanomaterial engineering have enabled the development of multi-enzyme mimetic nanozymes that exploit characteristic features of the tumor microenvironment, such as elevated hydrogen peroxide (H_2O_2) and glutathione (GSH) levels, to catalytically amplify intracellular oxidative stress [37–41]. Such catalytic ROS generation provides an opportunity to modulate tumor signaling networks and potentially enhance the efficacy of molecularly targeted therapies.

Herein, we developed a palbociclib-loaded Pt nanoparticle–decorated monolayer CoAl layered double hydroxide nanozyme (Palbo@Pt/m-CALDH) designed to enhance the therapeutic responsiveness of ESCC to CDK4/6 inhibition. The engineered nanosheets exhibit multiple enzyme-mimetic catalytic activities, including peroxidase (POD)-, oxidase (OXD)-, catalase (CAT)-, and glutathione oxidase (GSHOx)-like functions, enabling simultaneous ROS generation and intracellular glutathione depletion. This catalytic redox modulation markedly amplifies oxidative stress within tumor cells. Mechanistically, palbo treatment alone induced adaptive activation of MAPK and PI3K–AKT–mTOR signaling pathways together with increased expression of the ferroptosis regulator glutathione peroxidase 4 (GPX4). Nanozyme-mediated oxidative stress effectively suppressed these adaptive responses, thereby sensitizing ESCC tumors to CDK4/6 inhibition and enhancing antitumor efficacy both in vitro and in vivo (Scheme 1). Collectively, this work highlights the potential of catalytic nanozymes to modulate tumor redox signaling and provides a strategy for improving the therapeutic performance of CDK4/6 inhibitors in ESCC.

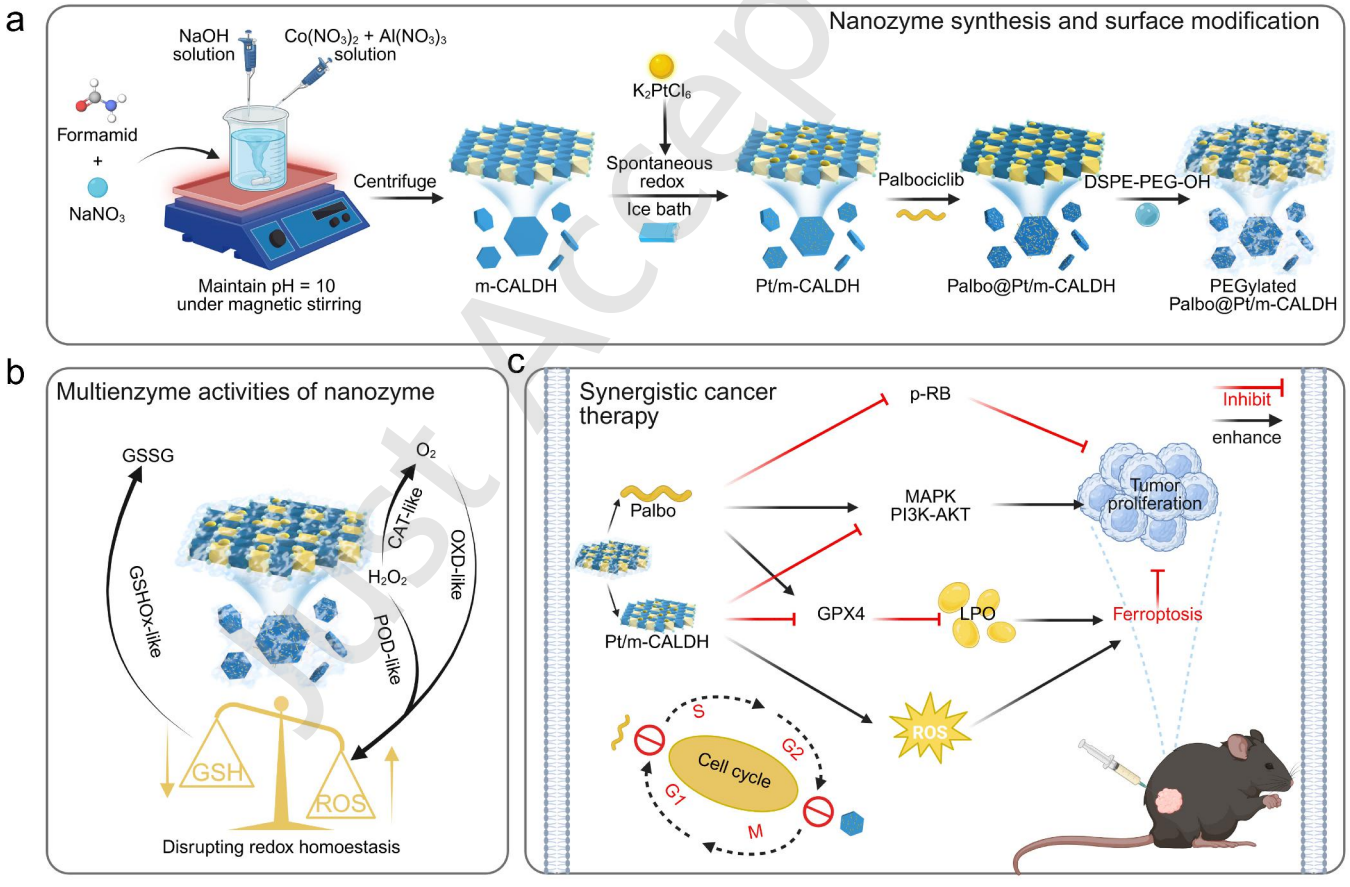

Scheme 1 (a) Schematic diagram of Pt/m-CALDH synthesis and surface modification. (b) Multi-enzyme mimic activity diagram of Pt/m-CALDH. (c) Schematic diagram of Pt/m-CALDH attenuating palbo-triggered adaptive responses.

2 Experimental

2.1 Materials

The details of the materials used in this study are described in the Supplementary Material.

2.2 Preparation of m-CALDH

Monolayer CoAl layered double hydroxide nanosheets were synthesized through a rapid coprecipitation process in a formamide-assisted aqueous system. Briefly, an aqueous solution containing $Co(NO_3)_2 \cdot 6H_2O$ (75 mM) and

$Al(NO_3)_3 \cdot 9H_2O$ (25 mM) was simultaneously introduced with NaOH solution (0.25 M) into a 23% formamide aqueous medium containing $NaNO_3$ (0.02 M) under vigorous stirring at 80 °C. The pH of the reaction system was maintained around 10. After approximately 10 min of reaction, ultrathin m-CALDH nanosheets were obtained by centrifugation and thoroughly washed with deionized water.

2.3. Preparation of Pt/m-CALDH

Pt nanoparticles were deposited onto m-CALDH nanosheets through an in-situ reduction process. Specifically, an aqueous solution of K_2PtCl_6 was slowly added to the m-CALDH dispersion under ice-bath conditions while stirring. After reacting for 10 min, the Pt-decorated nanosheets (Pt/m-CALDH) were collected by centrifugation (12000 rpm) and washed several times to remove residual precursors.

2.4 Preparation of PEGylated Palbo@Pt/m-CALDH

For drug loading, Pt/m-CALDH nanosheets were mixed with palbociclib in an aqueous solution containing DSPE-PEG-OH. The mixture was magnetically stirred for 12 h at low temperature to allow drug adsorption and surface PEGylation.
The resulting nanocomposite (Palbo@Pt/m-CALDH) was purified by repeated centrifugation and washing with deionized water. The final product was obtained after freeze-drying for further use.

2.5 Enzyme-mimicking catalytic activity assays

POD-like activity: POD-like activity was evaluated using TMB as the chromogenic substrate. Reaction mixtures containing Palbo@Pt/m-CALDH (10 μg mL^{-1}), H_2O_2 (1 mM), and TMB (1 mM) were prepared in sodium acetate buffer (0.1 M). The oxidation of TMB was monitored by measuring absorbance at 652 nm using UV-vis spectroscopy.
OXD-like activity: OXD-like catalytic activity was assessed by monitoring the oxidation of TMB in the absence of H_2O_2. Palbo@Pt/m-CALDH (10 μg mL^{-1}) was incubated with TMB in sodium acetate buffer, and the reaction progress was tracked by recording absorbance changes at 652 nm. Steady-state kinetic parameters were obtained by varying substrate concentrations and fitting the data to the Michaelis–Menten model.
GSHOx-like activity: the glutathione-consuming capability of the nanozyme was evaluated using a modified Ellman assay. GSH solution was incubated with Palbo@Pt/m-CALDH in PBS buffer (pH 6.5) at room temperature. After incubation, the remaining GSH was quantified by reacting the solution with DTNB reagent, and the absorbance of the resulting product was measured using UV-vis spectroscopy.
CAT-like activity: CAT-like activity was investigated by monitoring oxygen generation during H_2O_2 decomposition. Reaction mixtures containing H_2O_2, Palbo@Pt/m-CALDH, and the oxygen-sensitive probe $Ru(dpp)_3Cl_2$ were prepared in PBS buffer. Changes in fluorescence intensity of the probe were used to evaluate oxygen production.

2.6 ESR detection of ROS

ROS produced by the nanozyme were analyzed by ESR spectroscopy. DMPO was used as a spin-trapping agent for hydroxyl radicals (•OH) and superoxide radicals ($\bullet O_2^-$). Singlet oxygen ($^1O_2$) generation was detected using TEMP as the trapping probe.

2.7 Cellular uptake

AKR cells were incubated with Rhodamine B-labeled Palbo@Pt/m-CALDH (10 μg mL^{-1}) for 6 h. After washing with PBS, intracellular fluorescence distribution was observed using CLSM. For ultrastructural analysis, treated cells were fixed with glutaraldehyde, dehydrated with graded ethanol, embedded in resin, and sectioned for bio-TEM imaging.

2.8 Cell viability assay

Cell viability was determined using the CCK-8 assay. AKR cells were treated with Palbo, Pt/m-CALDH, or Palbo@Pt/m-CALDH (25 μg mL^{-1}) at various concentrations for 24 h. After incubation with CCK-8 reagent, absorbance was measured to evaluate cell viability.

2.9 CLSM imaging

Cells were treated with different formulations (25 μg mL^{-1}) for 24 h and subsequently stained with fluorescent probes for confocal imaging. Calcein-AM/PI staining was used to visualize live and dead cells. Intracellular ROS generation was monitored using DCFH-DA, while lipid peroxidation was evaluated using the C11-BODIPY581/591 probe. Intracellular GSH levels were visualized using a ThiolTracker Violet fluorescent probe. After incubation with the probes in the dark, fluorescence images were collected by confocal laser scanning microscopy.

2.10 Western blot

Cells were seeded in 6-well plates and allowed to adhere overnight. Cells were then treated with Palbo, Pt/m-CALDH, or Palbo@Pt/m-CALDH (25 μg mL^{-1}) for 24 h. After treatment, cells were washed with cold PBS and lysed using RIPA buffer supplemented with protease and phosphatase inhibitors. The protein concentration of each sample was determined using a BCA protein assay kit. Equal amounts of protein were separated by SDS–PAGE and subsequently transferred onto PVDF membranes. The membranes were blocked with 5% nonfat milk and incubated overnight at 4 °C with primary antibodies against the indicated proteins. After incubation with appropriate HRP-conjugated secondary antibodies, protein bands were quantified by ImageJ software.

2.11 RNA sequencing

Tumor tissues were collected from treated mice, immediately frozen in liquid nitrogen, and submitted to LC-Bio Technologies (Hangzhou) Co., Ltd. (China) for high-throughput mRNA sequencing and bioinformatic analysis according to the company's standard protocols.

2.12 Animal experiments

Female C57BL/6JNifdc mice (6 – 7 weeks old) were obtained from Sichuan Charles River Co., Ltd. All animal procedures were approved by the Ethics Committee of Sichuan University (Approval No. 20250521003). The AKR esophageal tumor model was established by subcutaneous injection of 1×10^6 AKR cells (100 μL) into the dorsal flank of mice. When the tumor volume reached approximately 120 mm^3, the mice were randomly divided

into four groups (n = 5) and treated by intratumoral injection: PBS (100 μL), Palbo (10 mg mL^{-1}, 100 μL), Pt/m-CALDH (10 mg mL^{-1}, 100 μL), and Palbo@Pt/m-CALDH (10 mg mL^{-1}, 100 μL). Treatments were administered on days 1, 3, 5, and 7. Tumor volume and body weight were recorded during the treatment period. Tumor volume was calculated using the equation: V = (length × $width^2$) / 2. After treatment, tumors and major organs were harvested for histological and immunohistochemical analyses.

2.13 Statistical analysis

All experiments were performed at least three times independently. Data are presented as mean ± standard deviation (SD). Statistical analysis was carried out using one-way ANOVA in GraphPad Prism 9.0. intergroup differences denoted as follows: *$p < 0.05$, **$p < 0.01$, and ***$p < 0.001$.

3 Results and discussion

The fabrication procedures of Pt/m-CALDH are illustrated in Scheme 1a. Monolayer CALDH nanosheets were first generated through an in-situ growth strategy in a formamide-containing aqueous system. Specifically, $Co(NO_3)_2$ and $Al(NO_3)_3$ precursor solutions were simultaneously introduced together with NaOH into a 23% formamide solution to induce the formation of ultrathin CALDH nanosheets. After purification by centrifugation and washing, K_2PtCl_6 was added into the dispersion, allowing Pt species to be reduced and deposited directly onto the nanosheet surface. Transmission electron microscopy (TEM) and high-resolution TEM (HRTEM) images (Fig. 1a-b) reveal nano-Pt anchored on the m-CALDH surface. The homogeneous distribution of Pt is further verified by high-angle annular dark-field scanning TEM (HAADF-STEM) combined with elemental mapping (Fig. 1c), where Pt signals are evenly distributed across the nanosheet framework. Atomic force microscopy (AFM) characterization (Fig. 1d) shows an average thickness of approximately 1.2 nm for m-CALDH, confirming its monolayer structure. The crystal structures of m-CALDH and Pt/m-CALDH were analyzed using X-ray diffraction (XRD). XRD patterns of Pt/m-CALDH and m-CALDH (Fig. 1e) both exhibited characteristic peaks corresponding to layered double hydroxides (JCPDS No.51-0045), while the absence of Pt diffraction peaks originated from low Pt loading and high dispersion of the nanoparticles. X-ray photoelectron spectroscopy (XPS) analysis confirmed the coexistence of Pt, Co, Al, and O (Fig. 1f). Deconvolution of the Co 2p spectrum (Fig. 1g) revealed peaks assigned to Co^{3+} and Co^{2+} species. Notably, the proportion of Co^{3+} increased from 49% in pristine m-CALDH to 56% after Pt deposition, suggesting that the spontaneous reduction of Pt^{4+} to Pt^0 was accompanied by partial oxidation of Co^{2+}.

To construct the therapeutic nanocomposite, palbo was loaded onto Pt/m-CALDH nanosheets in the presence or absence of the amphiphilic polymer DSPE-OH (Mw = 2000 Da), which serves to enhance colloidal stability and biocompatibility. This procedure yielded Palbo@Pt/m-CALDH and PEGylated Palbo@Pt/m-CALDH nanostructures. Zeta potential measurements (Fig. 1h) show that Pt/m-CALDH possess a positive charge of 29.7 mV, which is conducive to the loading of negatively charged drug. After palbo loading, the surface potential decreases to +12.9 mV, while subsequent PEGylation results in a charge reversal to −17.3 mV owing to the abundant methoxy groups in DSPE-OH. Hydrodynamic diameter analysis reveals size variations: Pt/m-CALDH (158.2 nm), Palbo@Pt/m-CALDH (228.1 nm), and PEGylated Palbo@Pt/m-CALDH (187 nm). The PEGylated Palbo@Pt/m-CALDH demonstrates an obvious size reduction, which will facilitate tumor targeting and enrichment through enhanced permeability and retention effects. For clarity in presentation, the terms Pt/m-CALDH and Palbo@Pt/m-CALDH in this work specifically denote their PEGylated nanocomposites, and unless otherwise specified, all experiments utilized PEGylated nanocomposites. UV-vis spectroscopy confirmed successful incorporation of palbo and DSPE-OH, with palbo loading efficiency was determined to be approximately 38% based on a standard calibration curve (Fig. S1). Furthermore, drug release studies demonstrated that palbo release from the nanocomposite is responsive to acidic conditions characteristic of the tumor microenvironment. Under acidic pH, palbo was gradually released, whereas negligible drug release was detected under neutral conditions (Fig. S2). In addition, the PEGylated nanocomposite maintained stable hydrodynamic size and surface charge during storage in PBS at 4 °C for one week and in serum-containing media for 24 h (Fig. 1i and S3), indicating good colloidal stability.

Considering that ROS play a central role in catalytic tumor therapy, electron spin resonance (ESR) spectroscopy was first employed to examine the ROS-generating capability of Palbo@Pt/m-CALDH. Using 5,5-dimethyl-1-pyrroline-N-oxide (DMPO) as the spin trapping agent, the introduction of H_2O_2 under acidic conditions produced a characteristic 1:2:2:1 quartet signal corresponding to hydroxyl radicals (•OH) (Fig. 1j). In contrast, in the absence of H_2O_2 under neutral conditions, ESR spectra displayed signals attributed to superoxide radicals ($•O_2^-$) (Fig. 1k). When 2,2,6,6-tetramethylpiperidine (TEMP) was used as the trapping probe, a typical 1:1:1 triplet signal corresponding to singlet oxygen ($^1O_2$) was observed (Fig. 1l). These results demonstrate that Palbo@Pt/m-CALDH can catalytically generate multiple ROS species.

Encouraged by these findings, we further examined the enzyme-mimetic catalytic activities of the nanozyme. The POD-like activity was first evaluated using 3,3′,5,5′-tetramethylbenzidine (TMB) as the chromogenic substrate. In the presence of H_2O_2, a strong absorption peak at 652 nm corresponding to oxidized TMB was observed (Fig. 1m), whereas the Pt-free nanosheets showed substantially weaker catalytic activity, confirming that Pt nanoparticles act as the primary catalytic centers. Kinetic analysis based on Michaelis–Menten modeling yielded a Km value of 1.92 mM and a Vmax of 4.17×10^{-7} $M·s^{-1}$ when H_2O_2 served as the substrate (Fig. S4). Using TMB as the substrate produced Km and Vmax values of 0.10 mM and 1.72×10^{-7} $M·s^{-1}$, respectively (Fig. S5). Similar to many reported POD-mimicking nanozymes, the catalytic activity of Palbo@Pt/m-CALDH increased under acidic conditions and decreased near neutral pH (Fig. S6), suggesting that the catalytic process can be activated within

the acidic tumor microenvironment and intracellular lysosomes. In addition to POD-like activity, the nanozyme also exhibited OXD-like catalytic behavior under acidic conditions. As shown in Fig. 1n, the characteristic oxTMB signal at 652 nm increased progressively with reaction time and nanozyme concentration, and Palbo@Pt/m-CALDH displayed stronger OXD-like activity compared with Pt-free nanosheets (Fig. S7). Kinetic analysis gave Km and Vmax values of 5.6 mM and 0.63 × 10^{-7} M·s^{-1}, respectively (Fig. S8).

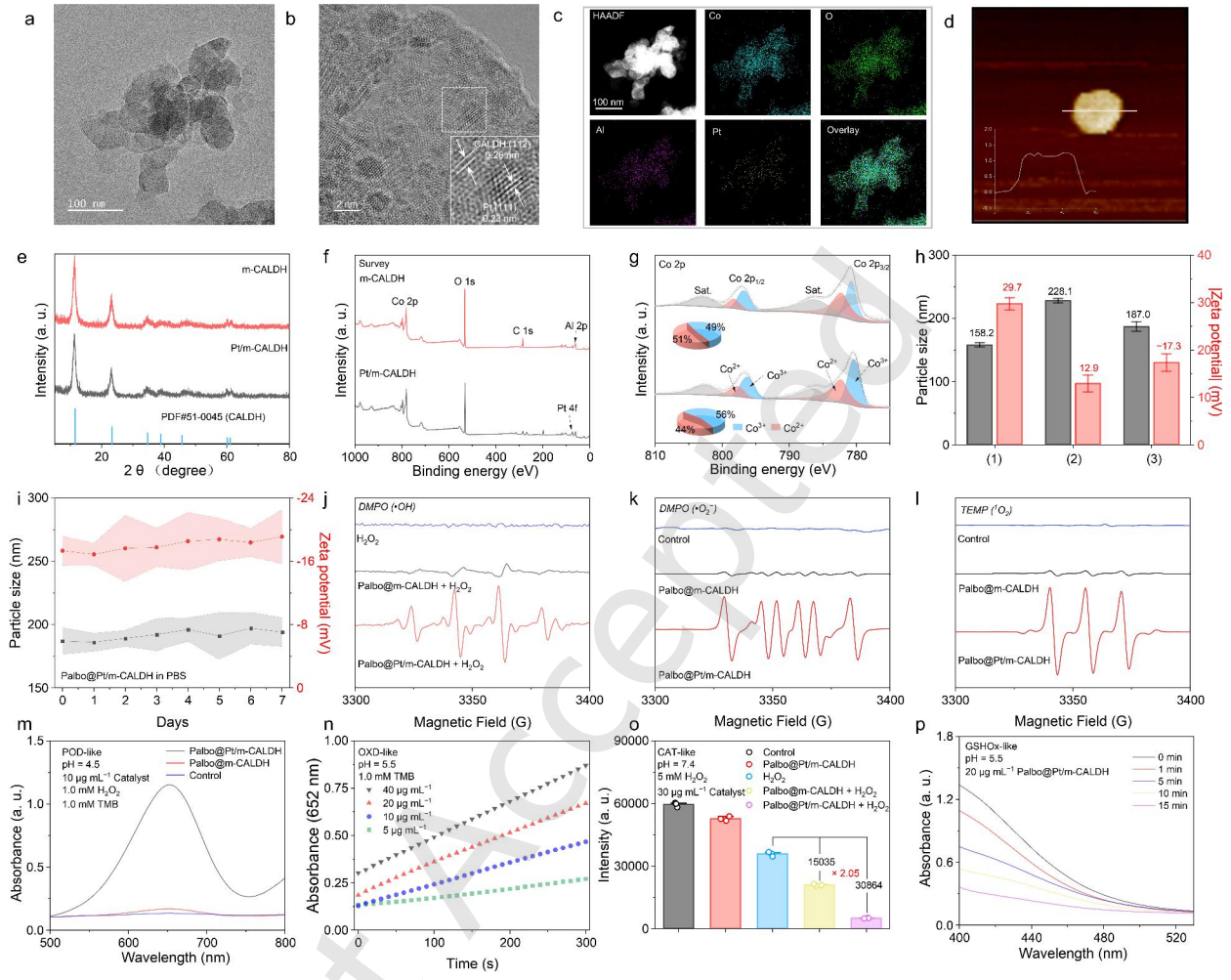

Figure 1 (a) TEM and (b) HRTEM images of Pt/m-CALDH. (c) EDX elemental mapping of Pt/m-CALDH. (d) AFM image of Pt/m-CALDH. (e) XRD patterns of m-CALDH and Pt/m-CALDH. (f) XPS survey spectrum and (g) high-resolution Co 2p spectrum of m-CALDH and Pt/m-CALDH. (h) Hydrodynamic diameters and zeta potentials of Pt/m-CALDH after different surface modifications. (i) Hydrodynamic diameters and zeta potentials of PEGylated Palbo@Pt/m-CALDH in PBS. ESR spectra for detection of (j) •OH, (k) $•O_2^-$, and (l) $^1O_2$ generated by Palbo@m-CALDH and Palbo@Pt/m-CALDH, respectively. (m) UV–vis spectra of oxTMB in different groups. (n) Time-dependent absorbance changes at 652nm in the presence of increasing concentrations of Palbo@Pt/m-CALDH. (o) Fluorescence intensity of oxygen sensor in different groups. (p) Time-dependent UV–vis spectra of DTNB in the presence of Palbo@Pt/m-CALDH.

Because tumor hypoxia is a major factor limiting therapeutic efficacy, we further investigated the CAT-like activity of the nanozyme. In the presence of H_2O_2, Palbo@Pt/m-CALDH rapidly catalyzed the decomposition of H_2O_2 into oxygen, which could be visually observed as bubble formation (Fig. S9). The generation of O_2 was further quantified using the oxygen-sensitive probe $[Ru(dpp)_3]^{2+}Cl_2$, whose fluorescence intensity decreases upon binding oxygen. Following treatment with Palbo@Pt/m-CALDH and H_2O_2, a marked reduction in fluorescence signal was observed, confirming efficient O_2 generation (Fig. 1o and S10). Although ROS production is beneficial for catalytic tumor therapy, intracellular GSH can effectively neutralize ROS and weaken oxidative stress–based treatments. Therefore, the ability of the nanozyme to deplete GSH was also investigated. Using the classical DTNB assay, the GSHOx-like activity of Palbo@Pt/m-CALDH was evaluated. In this reaction, GSH reduces DTNB to produce 2-nitro-5-mercaptobenzoic acid (TNB), and decreased TNB formation indicates GSH consumption. As shown in Fig. 1p, the absorbance of TNB gradually decreased with reaction time, indicating efficient GSH depletion by the nanozyme. Kinetic analysis revealed a Km value of 1.36 mM and a Vmax of 0.74 × 10^{-6} M·s^{-1} (Fig. S11).

As summarized in Scheme 1b, Palbo@Pt/m-CALDH integrates multiple enzyme-mimicking activities, including POD-, OXD-, CAT-, and GSHOx-like functions. Through these catalytic reactions, the nanozyme simultaneously generates ROS and depletes intracellular antioxidants, thereby

disrupting tumor redox balance and providing a foundation for ROS-mediated therapeutic applications.

Encouraged by the pronounced multienzyme-like catalytic properties observed in solution, we next investigated the antitumor performance of Palbo@Pt/m-CALDH in vitro. Efficient intracellular delivery of the nanozyme is a prerequisite for therapeutic activity; therefore, cellular uptake behavior was first examined. Bio-transmission electron microscopy (bio-TEM) images revealed clear structural differences between untreated mouse esophageal carcinoma (AKR) cells and cells exposed to the nanosheets, where electron-dense nanostructures were observed within intracellular vesicles, confirming successful endocytosis of Palbo@Pt/m-CALDH (Fig. 2a). Consistently, confocal laser scanning microscopy (CLSM) using rhodamine B–labeled nanosheets demonstrated progressive intracellular accumulation over time. Fluorescence signals increased continuously within 6 h of incubation, and semi-quantitative analysis further verified the time-dependent uptake process (Fig. 2b). Following confirmation of cellular internalization, the cytotoxic effects of the nanocomposite were systematically evaluated. Cell viability was first assessed using the Cell Counting Kit-8 (CCK-8) assay. As shown in Fig. 2c, Palbo@Pt/m-CALDH induces the most pronounced reduction in AKR cell viability compared with the other treatment groups, suggesting enhanced antitumor activity resulting from the combined effects of palbo and nanozyme-mediated catalysis. The combination index (CI) analysis demonstrated a strong synergistic interaction between palbo and Pt/m-CALDH, with CI values consistently below 0.5, indicating strong cooperative antitumor activity between palbo and the nanozyme (Fig. S12). Importantly, all treatment groups exhibited minimal cytotoxicity toward the normal esophageal epithelial cell line Het-1A even at relatively high concentrations, indicating favorable biocompatibility. Similar trends were observed in the colony formation assay, where Palbo@Pt/m-CALDH treatment led to the most substantial suppression of long-term proliferative capacity in tumor cells (Fig. 2d).

To further visualize therapeutic efficacy at the cellular level, Calcein AM/propidium iodide (PI) dual staining was performed to distinguish live and dead cells. CLSM imaging reveals strong green fluorescence corresponding to viable cells in the control and palbo groups, whereas extensive red fluorescence indicative of dead cells is observed following treatment with Palbo@Pt/m-CALDH (Fig. 2e). Quantitative fluorescence analysis further confirmed the superior cytotoxic effect of the nanocomposite (Fig. 2f). Because catalytic ROS generation is the key mechanism underlying nanozyme-based therapy, intracellular oxidative stress was subsequently evaluated using the ROS-sensitive probe 2,7-dichlorodihydrofluorescein diacetate (DCFH-DA). CLSM images showed negligible fluorescence in the control and palbo groups, while markedly stronger green fluorescence signals were detected in the Pt/m-CALDH and Palbo@Pt/m-CALDH groups, indicating increased ROS production (Fig. 2g). Flow cytometric analysis further verified these observations and revealed that Palbo@Pt/m-CALDH treatment generated the highest intracellular ROS levels among all groups (Fig. 3h).

Considering the good CAT-like activity of the nanozyme, we next investigated its ability to modulate intracellular oxygen levels. The oxygen-sensitive probe $[Ru(dpp)_3]^{2+}Cl_2$ was used for detection, as its fluorescence intensity decreases in the presence of oxygen. Compared with the other groups, the Palbo@Pt/m-CALDH-treated cells exhibited significantly reduced red fluorescence, suggesting effective oxygen generation inside the cells (Fig. 3i). Quantitative fluorescence analysis supported the enhanced oxygenation effect of the nanozyme (Fig. 3j). Finally, apoptosis induction was analyzed using Annexin V-FITC/PI staining followed by flow cytometry. Cells treated with Palbo@Pt/m-CALDH displayed markedly elevated apoptotic populations compared with all control groups. Specifically, early apoptotic cells (Q3), late apoptotic cells (Q2), and total apoptotic cells (Q2 + Q3) reached 26.6%, 44%, and 66.6%, respectively, highlighting the strong pro-apoptotic effect of the combined nanozyme and palbo treatment (Fig. 2k–i). To further clarify the contribution of ROS to cell death, N-acetylcysteine (NAC), a classical ROS scavenger, was introduced. As revealed by the CCK-8 assay, NAC treatment significantly restored cell viability, highlighting the pivotal role of ROS in the cytotoxic effect (Fig. S13).

Given the potential interplay between oxidative stress and oncogenic signaling pathways, we next investigated whether the PI3K–AKT–mTOR and MAPK cascades contribute to the limited responsiveness of ESCC cells to palbo. We first examined the key components within the CDK4/6 signaling axis. Under physiological conditions, the cyclin D1–CDK4/6 complex phosphorylates the retinoblastoma (RB) protein, leading to the release of E2F transcription factors and subsequent activation of genes required for S-phase entry. Palbo inhibits CDK4/6 by occupying the ATP-binding pocket of the cyclin D–CDK4/6 complex, thereby preventing RB phosphorylation and inducing G1-phase cell cycle arrest [42–44]. Western blot analysis (Fig. 3a) confirmed that palbo treatment effectively reduced the phosphorylation level of RB while simultaneously inducing upregulation of CDK4/6 and cyclin D1. In contrast, treatment with Pt/m-CALDH resulted in decreased expression of CDK4/6, CCND1, and p-RB. In the combination group, Palbo@Pt/m-CALDH moderately increased these proteins compared with the Pt/m-CALDH group but maintained lower expression levels than those observed under palbo monotherapy, suggesting cooperative regulation of the CDK4/6 pathway by the nanozyme and palbo.

Cell cycle distribution was further analyzed by flow cytometry. As shown in Fig. 3c and S14, palbo treatment markedly increased the proportion of cells in the G0/G1 phase, consistent with CDK4/6 inhibition. In contrast, Pt/m-CALDH treatment induced accumulation of cells in the G2/M phase, which may be attributed to ROS-induced DNA damage. Notably, the Palbo@Pt/m-CALDH group exhibited a pronounced reduction in the S-phase population compared with either monotherapy group, indicating enhanced blockade of cell cycle progression through simultaneous interference with both the G1/S and G2/M checkpoints. To further verify

ROS-mediated genomic stress, γ-H2AX immunofluorescence staining was

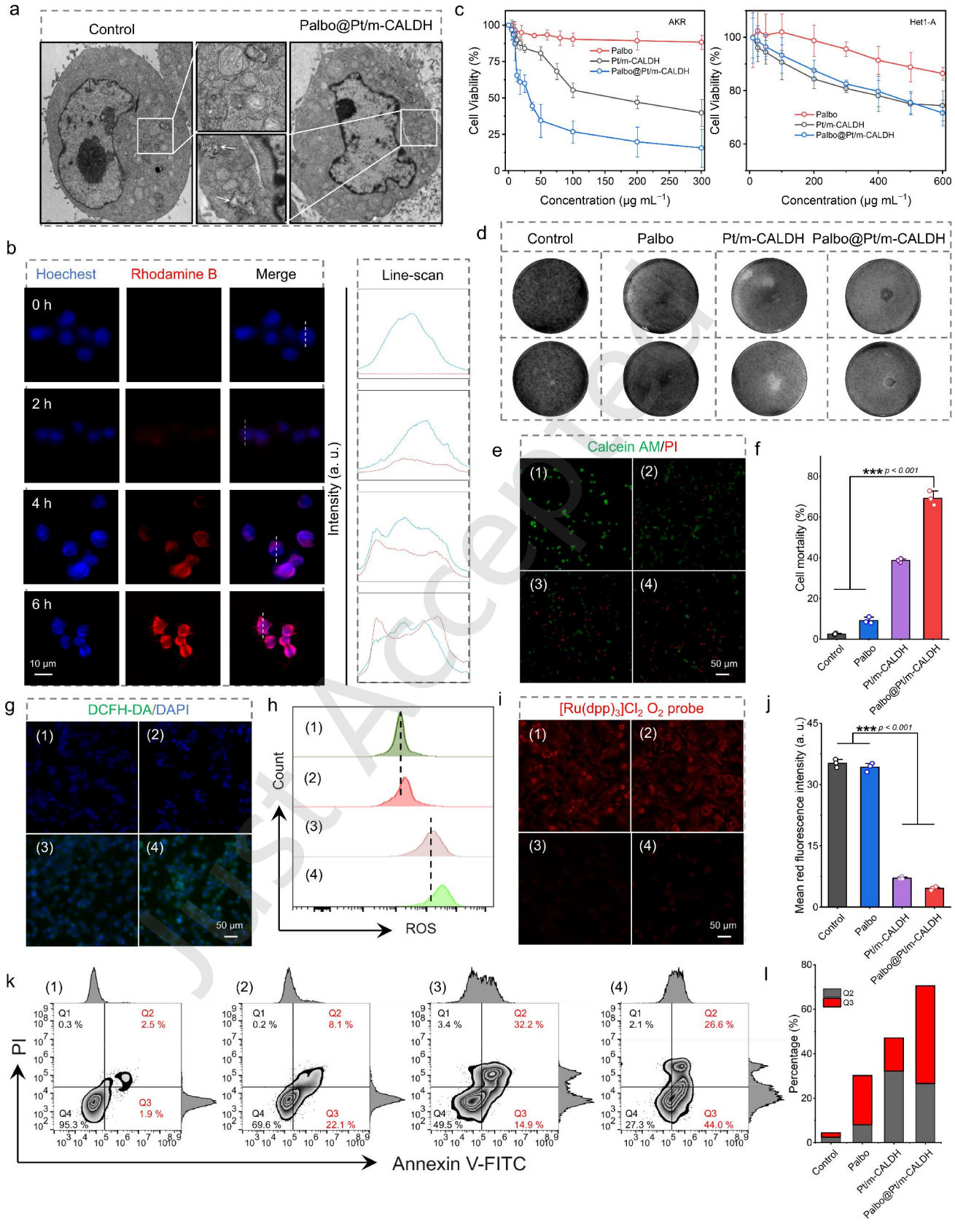

Figure 2 (a) Bio-TEM images of AKR cell after incubation with Palbo@Pt/m-CALDH. (b) Time-dependent CLSM images and profiles of AKR cells treated with Rhodamine B-labeled Palbo@Pt/m-CALDH. (c) CCK-8 assays of different treatment to AKR and Het-1A cells. (d) Colony formation assays after different treatments. (e) Live/dead staining of AKR cells and (f) corresponding quantitative analysis. (g) ROS staining of AKR cells. (h) Flow cytometric analysis of ROS levels. (i) O_2 probe staining of AKR cells and (k) corresponding quantitative analysis. (k) Apoptosis analysis using Annexin

V-APC and PI staining and (l) corresponding quantitative results. Groups: 1 Control, 2 Palbo, 3 Pt/m-CALDH, and 4 Palbo@Pt/m-CALDH. Data are presented as mean ± S.D. (n = 3), **p < 0.01, ***p < 0.001.

performed to detect DNA double-strand breaks. Strong fluorescence signals were observed in both the Pt/m-CALDH and Palbo@Pt/m-CALDH groups (Fig. S15), confirming substantial DNA damage induced by nanozyme-generated oxidative stress. These findings suggest that palbo restricts tumor cells from entering

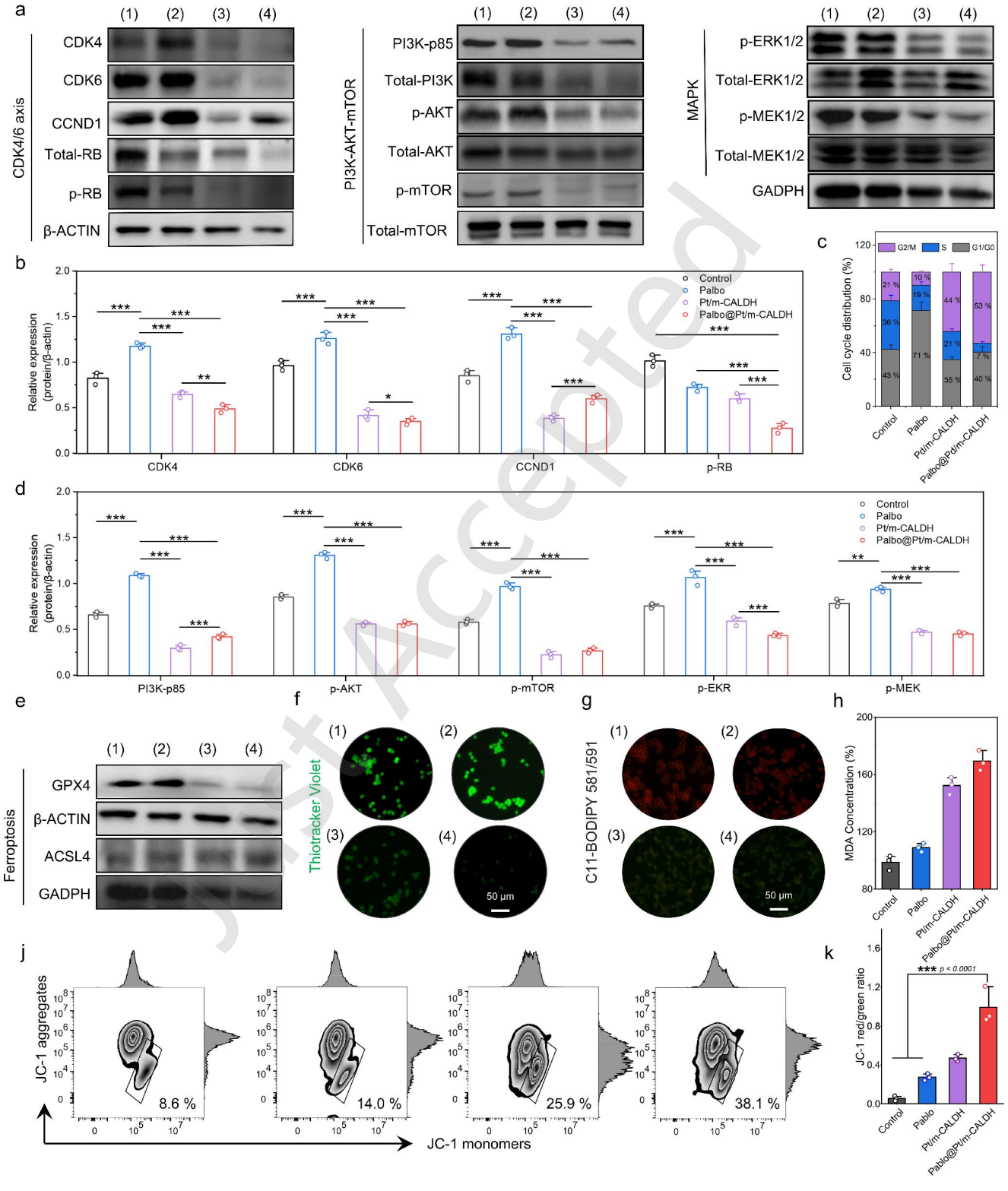

Figure 3 (a) Western blot analysis of proteins involved in the CDK4/6 axis, PI3K-AKT-mTOR, and MAPK signaling pathways, with (b, d) corresponding quantitative analysis. (c) Flow cytometric quantification of cell-cycle distribution under different treatments. (e) Western blot analysis of ferroptosis related proteins. (f) GSH levels and (g) LPO levels staining of AKR cells. (h) MDA concentrations after different treatment. (j) Mitochondrial membrane potential analysis using JC-1 staining and (k) corresponding quantitative results. Groups: 1 Control, 2 Palbo, 3 Pt/m-CALDH, and 4 Palbo@Pt/m-CALDH. Data are presented as mean ± S.D. (n = 3), **p < 0.01, ***p < 0.001.

Nano Research
ISSN 1998-0124 CN 11-5974/O4
https://doi.org/10.26599/NR.2026.94908832

S-phase, while the ROS produced by the nanozyme imposes additional replication stress, ultimately reinforcing cell cycle arrest.

We next examined the activation status of the PI3K–AKT–mTOR and MAPK signaling pathways. Western blot analysis (Fig. 3a and 3d) showed that palbo monotherapy increased the phosphorylation levels of several key proteins within these pathways, suggesting the presence of compensatory feedback activation that may limit the therapeutic efficacy of CDK4/6 inhibition. In contrast, oxidative stress generated by Pt/m-CALDH significantly suppressed the phosphorylation of these signaling components. Although partial recovery of phosphorylation was observed in the Palbo@Pt/m-CALDH group compared with Pt/m-CALDH alone, the overall activation levels remained substantially lower than those detected in untreated cells. Collectively, these results indicate that the nanozyme effectively attenuates palbociclib-induced adaptive signaling responses, thereby enhancing the antitumor activity of CDK4/6 inhibition. Notably, this suppression primarily affected phosphorylated proteins without significantly altering the expression levels of their corresponding total proteins, highlighting a signaling-level regulatory mechanism.

Considering the pronounced oxidative stress induced by Pt/m-CALDH, we further explored whether additional forms of regulated cell death were involved. Ferroptosis is a non-apoptotic form of cell death characterized by iron-dependent accumulation of lipid peroxides (LPO) and dysfunction of the antioxidant enzyme GPX4. In this process, ROS initiates lipid peroxidation by attacking polyunsaturated fatty acids, generating lipid radicals that subsequently react with molecular oxygen to form lipid peroxyl radicals. These intermediates ultimately produce lipid hydroperoxides (LOOH), which can further decompose into reactive aldehydes such as malondialdehyde (MDA). GPX4 plays a central role in suppressing ferroptosis by utilizing GSH to detoxify LOOH and interrupt the lipid peroxidation chain reaction. Another important ferroptosis-associated enzyme is long-chain acyl-CoA synthetase 4 (ACSL4), which promotes the biosynthesis of polyunsaturated phospholipids that serve as substrates for lipid peroxidation.

Western blot analysis revealed that palbo treatment increased GPX4 expression in ESCC cells, suggesting the activation of an antioxidant defense mechanism that may contribute to reduced sensitivity to CDK4/6 inhibition. In contrast, the Palbo@Pt/m-CALDH group exhibited markedly decreased GPX4 expression together with elevated ACSL4 levels compared with both the control and palbo groups, indicating activation of ferroptotic signaling (Fig. 3e and S16). Given that GPX4 activity is critically dependent on intracellular glutathione, GSH levels were subsequently measured. Consistent with GPX4 expression patterns, palbo-treated cells displayed the highest intracellular GSH levels, whereas the Pt/m-CALDH group showed the most pronounced GSH depletion (Fig. S17). Visualization of intracellular thiols using the ThiolTracker Violet probe further supported these observations. Strong fluorescence signals were detected in the palbo-treated cells, whereas negligible fluorescence was observed in the Pt/m-CALDH group (Fig. 3f), indicating extensive depletion of intracellular GSH.

To directly evaluate LPO, the C11-BODIPY581/591 probe was used to monitor LPO levels based on fluorescence emission shifts from red (590 nm) to green (510 nm). Treatment with Palbo@Pt/m-CALDH significantly increased the green/red fluorescence ratio, indicating elevated lipid peroxide accumulation (Fig. 3g and 3h). Consistently, quantitative measurement of MDA (Fig. 3i), a downstream product of lipid peroxidation, confirmed enhanced LPO levels following nanozyme treatment. Because mitochondrial dysfunction is closely associated with both apoptosis and ferroptosis [45], mitochondrial membrane potential changes were assessed using the JC-1 assay. The results demonstrated significant disruption of mitochondrial membrane potential in cells treated with Palbo@Pt/m-CALDH, further supporting the induction of oxidative stress–mediated cell death pathways (Fig. 3j and 3k).

To further validate the therapeutic performance of Palbo@Pt/m-CALDH in vivo, we established a subcutaneous tumor model by inoculating AKR cells into the right flank of C57BL/6 mice. We first evaluated the compatibility of Palbo@Pt/m-CALDH with red blood cells. Hemolysis assays showed no significant hemolysis at concentrations up to 500 μg mL^{-1}, indicating good blood compatibility (Fig. S18). When tumors reached an average volume of approximately 120 mm^3, the mice were randomly assigned to four treatment groups (n = 5 per group): PBS control, Palbo, Pt/m-CALDH, and Palbo@Pt/m-CALDH. All formulations were administered via intratumoral injection (100 μL, 10 mg mL^{-1}) according to the treatment schedule illustrated in Fig. 4a. Tumor growth was monitored over a 10-day therapeutic window to evaluate the antitumor efficacy of the different treatments. Tumors in the control group expanded rapidly, whereas monotherapy with either palbo or Pt/m-CALDH produced only modest growth delay. In contrast, the combination formulation Palbo@Pt/m-CALDH resulted in pronounced tumor suppression, indicating a clear synergistic therapeutic benefit derived from the integration of CDK4/6 inhibition and nanozyme-mediated oxidative stress (Fig. 4b and Fig. S19). Consistent with the tumor growth curves, the excised tumor masses and representative photographs further corroborated the superior tumor-inhibitory activity of the combined treatment (Fig. 4c). Throughout the treatment period, mice maintained stable body weights without noticeable fluctuations (Fig. S20), while histological analysis hematoxylin and eosin (HE) of major organs revealed no pathological abnormalities (Fig. S21). Moreover, serum biochemical parameters remained within normal physiological ranges, suggesting that Palbo@Pt/m-CALDH exhibits acceptable systemic biosafety (Fig. 4d).

Histological examination of tumor sections provided additional mechanistic insight. HE staining revealed well-preserved tissue architecture in the control tumors, whereas extensive structural disruption and cellular damage were observed in the Palbo@Pt/m-CALDH-treated tumors.

The therapeutic effect was further substantiated by terminal deoxynucleotidyl transferase dUTP nick-end labeling (TUNEL) and Ki67 immunostaining. The Palbo@Pt/m-CALDH group displayed markedly enhanced apoptotic signals together with a substantial reduction in Ki67 expression, reflecting strong pro-apoptotic and antiproliferative activities. Consistent with the cellular studies, immunofluorescence analysis demonstrated that GPX4 expression was markedly elevated in tumors treated with palbo alone, whereas the Palbo@Pt/m-CALDH group exhibited pronounced suppression of GPX4 signals, further highlighting the critical role of GPX4-mediated antioxidant defense in palbo treatment. Meanwhile, tumors receiving palbo monotherapy showed increased levels of p-AKT and p-ERK, indicative of compensatory activation of the PI3K-AKT and MAPK pathways. Importantly, these resistance-associated signaling events were effectively attenuated in the Palbo@Pt/m-CALDH group, confirming that nanozyme-induced oxidative stress sensitizes tumors to CDK4/6 inhibition by disrupting adaptive survival signaling (Fig. 4e).

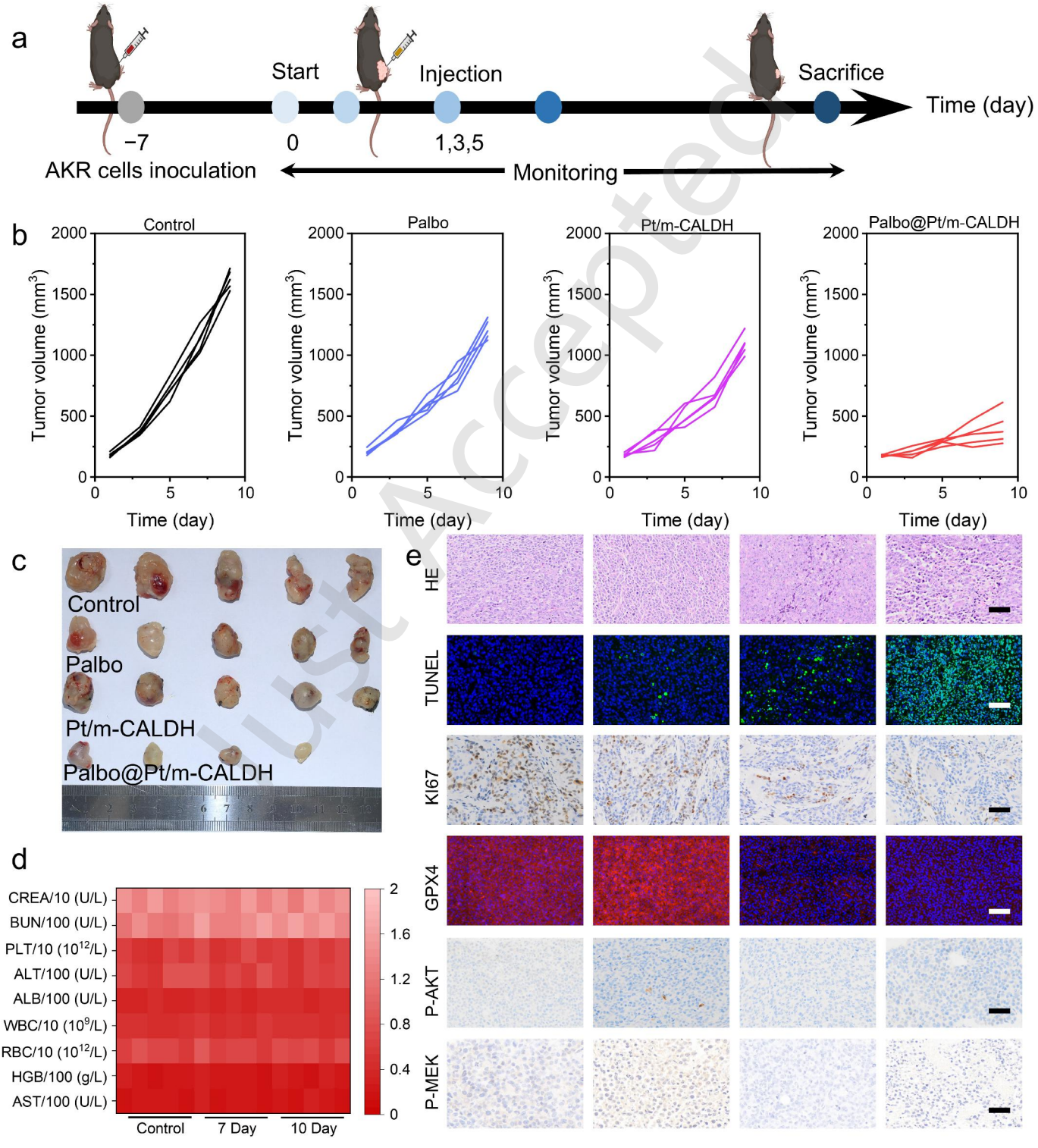

Figure 4 (a) Schematic illustration of the treatment protocol in AKR tumor-bearing mice. (b) Tumor growth curves of different treatment groups. (c) Photographs of excised tumors collected at the end of treatment. (d) Blood biochemical parameters of mice in the Palbo@Pt/m-CALDH treatment group. HE, TUNEL, Ki67, GPX4, p-AKT, and p-MEK staining of tumor sections obtained from mice in different treatment groups (scale bar: 50 μm). Data are presented as mean ± S.D. (n = 3), **p < 0.01, ***p < 0.001.

To elucidate the synergistic antitumor mechanism of Palbo@Pt/m-CALDH, RNA sequencing was performed to analyze the transcriptomic profiles of tumor tissues from mice treated with PBS, Palbo, Pt/m-CALDH, or Palbo@Pt/m-CALDH. The heatmap of differentially expressed genes (DEGs) and principal component analysis (PCA) revealed clear transcriptomic differences among the treatment groups (Fig. 5a and S22). Venn diagrams and multi-group volcano plots demonstrated substantial transcriptomic alterations across different treatments (Fig. 5b and 5c). Notably, reversal gene expression analysis indicated that Palbo@Pt/m-CALDH markedly reshaped the gene expression patterns induced by palbo (Fig. 5d and S23). According to the Gene Ontology database, the DEGs induced by Palbo@Pt/m-CALDH were mainly enriched in categories related to molecular function, biological process, and cellular components (Fig. S24). Further Kyoto Encyclopedia of Genes and Genomes (KEGG) pathway enrichment analysis identified several signaling pathways associated with Palbo@Pt/m-CALDH treatment, including the PI3K-AKT-mTOR pathway, MAPK signaling, as well as pathways related to ROS, ferroptosis, and cell cycle (Fig. 1f and 1g). These findings were further validated by gene set enrichment analysis (GSEA) (Fig. 1e). Collectively, the RNA-seq results further support the drug-sensitization strategy of Pt/m-CALDH, in which nanozyme-mediated oxidative stress effectively suppresses adaptive cellular responses, thereby sensitizing ESCC tumors to CDK4/6 inhibition and enhancing the antitumor efficacy both in vitro and in vivo.

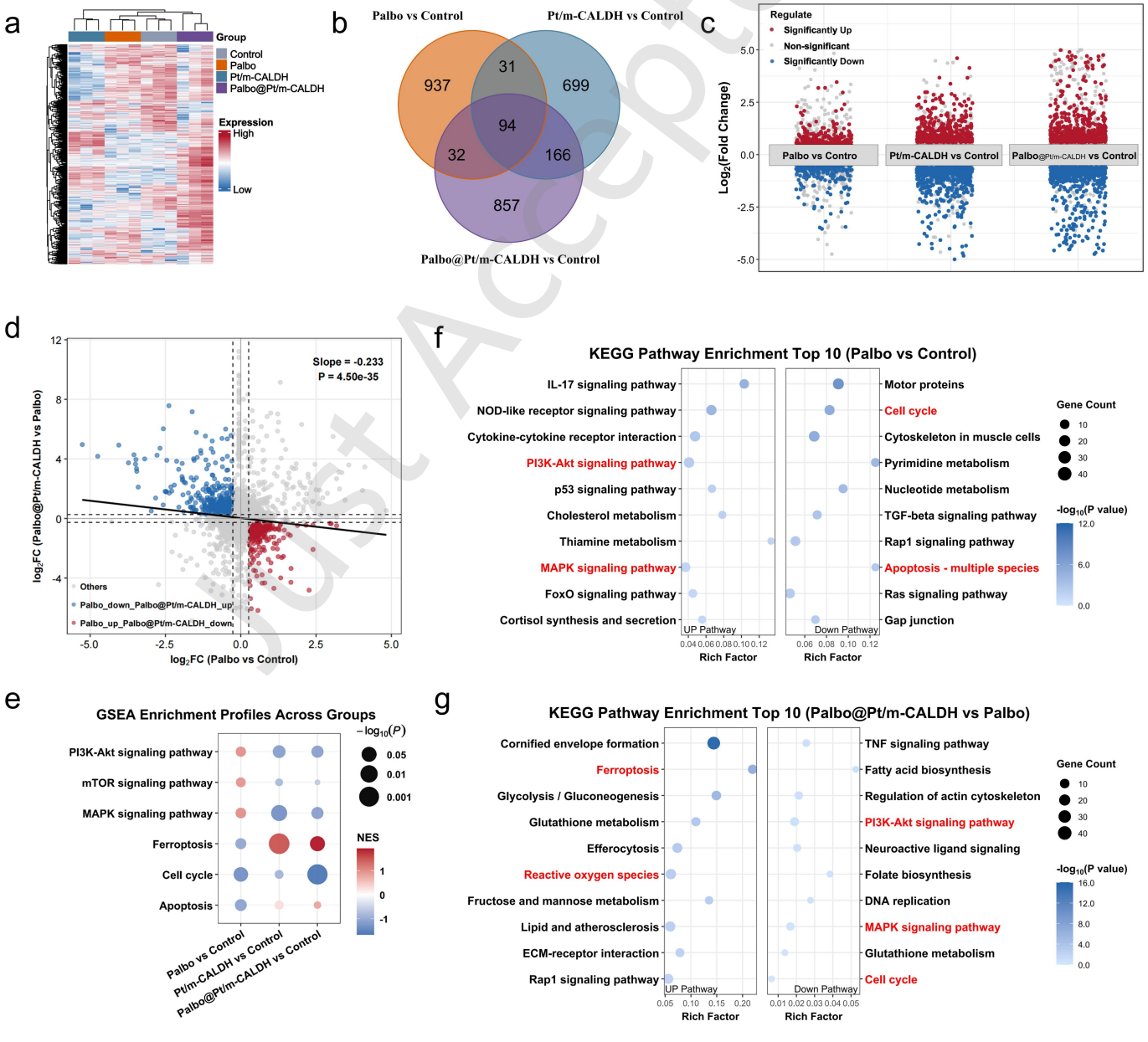

Figure 5 (a)Heat map of DEGs screened in different samples. (b) Venn diagram of different samples. (c) Multi group volcanic plot of DEGs in different samples. (d) Reversal gene expression analysis between Palbo@Pt/m-CALDH and Palbo groups. (e) GSEA enrichment analysis of different pathways. (f, g) KEGG pathway enrichment analysis of the down-regulated and up-regulated pathways.

4 Conclusions

In summary, we developed a palbo-loaded nanozyme to enhance the therapeutic responsiveness of ESCC to CDK4/6 inhibition. The nanosheet integrates multiple enzyme-mimicking catalytic activities, enabling simultaneous ROS amplification, oxygen generation, and intracellular glutathione depletion, thereby disrupting tumor redox homeostasis. The nanozyme-mediated oxidative stress effectively suppresses palbo-induced adaptive responses, including compensatory activation of the PI3K–AKT–mTOR and MAPK pathways and upregulation of GPX4, while promoting ferroptosis-associated LPO. Through coordinated regulation of redox balance and oncogenic signaling, the nanozyme markedly enhances the antitumor efficacy of palbo both in vitro and in vivo. Collectively, this work highlights catalytic redox modulation by nanozymes as a promising strategy for durg sensitizing to molecularly targeted therapies and provides a potential therapeutic framework for ESCC treatment.

Electronic Supplementary Material: Supplementary material is available in the online version of this article at https://doi.org/10.26599/NR.2026.94908832.

Data availability

The original contributions presented in the study are included inthe article and the Electronic Supplementary Materials, further inquiries can be directed to the corresponding author.

Acknowledgements

This work was supported by grants from the Natural Science Foundation of China (Nos. 82273018, 82272685, 82472745, and 82472346), the Noncommunicable Chronic Diseases-National Science and Technology Major Project of China (2025ZD0552413, 2025ZD0552312), the Science and Technology Department of Sichuan Province (2024NSFSC0734, and 1 3 5 project for disciplines of excellence-Clinical Research Fund, West China Hospital, Sichuan University (2025HXFH027) and Key Research and Development Science and Technology Program Project for High-Quality Development 2024 of The First People's Hospital of Zigong City (2024GZL03). The authors extend their appreciation to the Deanship of Scientific Research, Islamic University of Madinah, Saudi Arabia, for funding this research work.

Declaration of competing interest

The authors declare no conflict of interest.

Author contribution statement

L.L., Y.L. X.S., and J.Z. designed this research. L.L., J.F. and Y.L. wrote the manuscript. L.L., J.F. and Y.L. performed material synthesis, characterizations, and performance test. L.L., J.F. and Y.L. analyzed the experimental and theoretical data. L.L., Y.L. X.S., and J.Z. supervised the research. All authors contributed and reviewed the manuscript.

Informed consent

Not applicable.

Ethics statement

Not applicable.

Use of AI statement

None

References

[1] Bray, F.; Laversanne, M.; Sung, H.; Ferlay, J.; Siegel, R. L.; Soerjomataram, I.; Jemal, A. Global cancer statistics 2022: GLOBOCAN estimates of incidence and mortality worldwide for 36 cancers in 185 countries. *CA-Cancer Jo. Clin.* **2024**, *74*, 229–263.

[2] Deboever, N.; Jones, C. M.; Yamashita, K.; Ajani, J. A.; Hofstetter, W. L. Advances in diagnosis and management of cancer of the esophagus. *BMJ* **2024**, *385*, e074962.

[3] Henick, B. S.; Taylor, A. M.; Nakagawa, H.; Wong, K.-K.; Diehl, J. A.; Rustgi, A. K. Squamous cell Cancers of the Aero-upper digestive tract: A unified perspective on biology, genetics, and therapy. *Cancer Cell*. **2025**, *44*, 178–194.

[4] Jiang, W.; Zhang, B.; Xu, J.; Xue, L.; Wang, L. Current status and perspectives of esophageal cancer: A comprehensive review. *Cancer Commun.* **2025**, *45*, 281–331.

[5] Yang, H.; Wang, F.; Hallemeier, C. L.; Lerut, T.; Fu, J. Oesophageal Cancer. *Lancet* **2024**, *404*, 1991–2005.

[6] Qu, H.-T.; Li, Q.; Hao, L.; Ni, Y.-J.; Luan, W.-Y.; Yang, Z.; Chen, X.-D.; Zhang, T.-T.; Miao, Y.-D.; Zhang, F. Esophageal cancer screening, early detection and treatment: Current insights and future directions. *World J. Gastrointest. Oncol.* **2024**, *16,*1180-1191.

[7] Sheikh, M.; Roshandel, G.; McCormack, V.; Malekzadeh, R. Current status and future prospects for esophageal cancer. *Cancers* **2023**, *15*, 765.

[8] Rached, L.; Laparra, A.; Sakkal, M.; Danlos, F.-X.; Barlesi, F.; Carbonnel, F.; De Martin, E.; Ducreux, M.; Even, C.; Le Pavec, J.; et al. Toxicity of immunotherapy combinations with chemotherapy across tumor indications: Current knowledge and practical recommendations. *Cancer Treat. Rev.* **2024**, *127*, 102751.

[9] Zhan, T.; Betge, J.; Schulte, N.; Dreikhausen, L.; Hirth, M.; Li, M.; Weidner, P.; Leipertz, A.; Teufel, A.; Ebert, M. P. Digestive cancers: Mechanisms, therapeutics and management. *Sig. Transduct. Target Ther.* **2025**, *10*, 24.

[10] Kalra, A.; Meltzer, S. J. The Role of DNA methylation in Gastrointestinal disease: An expanded review of malignant and nonmalignant gastrointestinal diseases. *Gastroenterology* **2025**, *168*, 245–266.

[11] Kim, J.; Bowlby, R.; Mungall, A. J.; Robertson, A. G.; Odze, R. D.; Cherniack, A. D.; Shih, J.; Pedamallu, C. S.; Cibulskis, C.; Dunford, A.; et al. Integrated genomic characterization of oesophageal carcinoma. *Nature* **2017**, *541*, 169–175.

[12] Gao, J.; Wang, Q.; Fu, F.; Zhao, Y.; Yang, T.; Li, X.; Sun, Y.; Hu, H.; Ma, L.; Miao, L.; et al. Comprehensive

genomic and transcriptomic analyses reveal prognostic stratification for esophageal squamous cell carcinoma. *Sig. Transduct. Target Ther.* **2025**, *10*, 223.

[13] Yuan, P.; Rao, W.; Lin, Z.; Liu, S.; Lin, X.; Wu, C.; Lin, X.; Hu, Z.; Ye, W. Genomic analyses reveal SCN7A is associated with the prognosis of esophageal squamous cell carcinoma. *Esophagus* **2022**, *19*, 303–315.

[14] Frankell, A. M.; Jammula, S.; Li, X.; Contino, G.; Killcoyne, S.; Abbas, S.; Perner, J.; Bower, L.; Devonshire, G.; Ococks, E.; et al. The landscape of selection in 551 esophageal adenocarcinomas defines genomic biomarkers for the clinic. *Nat. Genet.* **2019**, *51*, 506–516.

[15] Abnet, C. C.; Arnold, M.; Wei, W.-Q. Epidemiology of esophageal squamous cell carcinoma. *Gastroenterology* **2018**, *154*, 360–373.

[16] Kudo, R.; Safonov, A.; Jones, C.; Moiso, E.; Dry, J. R.; Shao, H.; Nag, S.; da Silva, E. M.; Yildirim, S. Y.; Li, Q.; et al. Long-Term breast cancer response to CDK4/6 inhibition defined by TP53-Mediated geroconversion. *Cancer Cell* **2024**, *42*, 1919–1935.

[17] Goel, S.; Wang, Q.; Watt, A. C.; Tolaney, S. M.; Dillon, D. A.; Li, W.; Ramm, S.; Palmer, A. C.; Yuzugullu, H.; Varadan, V.; et al. Overcoming therapeutic resistance in HER2-positive breast cancers with CDK4/6 Inhibitors. *Cancer Cell* **2016**, *29*, 255–269.

[18] Sonke, G. S.; van Ommen-Nijhof, A.; Wortelboer, N.; van der Noort, V.; Swinkels, A. C. P.; Blommestein, H. M.; Paez, C. G.; Mol, L.; Beeker, A.; Beelen, K.; et al. Early versus deferred use of CDK4/6 inhibitors in advanced breast cancer. *Nature* **2024**, *636*, 474–480.

[19] Karasic, T. B.; O'Hara, M. H.; Teitelbaum, U. R.; Damjanov, N.; Giantonio, B. J.; d'Entremont, T. S.; Gallagher, M.; Zhang, P. J.; O'Dwyer, P. J. Phase II trial of palbociclib in patients with advanced esophageal or gastric cancer. *Oncologist* **2020**, *25*, e13453.

[20] Morrison, L.; Loibl, S.; Turner, N. C. The CDK4/6 inhibitor revolution — a game-changing era for breast cancer treatment. *Nat. Rev. Clin. Oncol.* **2024**, *21*, 89–105.

[21] Lloyd, M. R.; Jhaveri, K.; Kalinsky, K.; Bardia, A.; Wander, S. A. Precision therapeutics and emerging strategies for HR-positive metastatic breast cancer. *Nat. Rev. Clin. Oncol.* **2024**, *21*, 743–761.

[22] Xu, H.; Yu, S.; Liu, Q.; Yuan, X.; Mani, S.; Pestell, R. G.; Wu, K. Recent advances of highly selective CDK4/6 inhibitors in breast cancer. *J. Hematol. Oncol.*, **2017**, *10*, 97.

[23] Yang, J.; Wang, S.; Li, X.; Xu, H.; Sun, T.; Hu, T.; Luo, J.; Zhou, H. Signaling pathways and targeted interventions for precancers. *Sig. Transduct. Target Ther.* **2026**, *11*, 9.

[24] Shimizu, T.; Tolcher, A. W.; Papadopoulos, K. P.; Beeram, M.; Rasco, D. W.; Smith, L. S.; Drengler, R. L.; Gunn, S.; Smetzer, L.; Mays, T. A.; et al. Personalizing cancer treatment of combined targeting of PI3K/AKT and MAPK Pathways in advanced cancer patients harboring simultaneous oncogenic alterations in both signaling pathways. *J. Clin. Oncol.* **2012**, *30*, e13025.

[25] Tian, Y.; Chen, Z.-H.; Wu, P.; Zhang, D.; Ma, Y.; Liu, X.-F.; Wang, X.; Ding, D.; Cao, X.-C.; Yu, Y. MIR497HG-Derived miR-195 and miR-497 mediate tamoxifen resistance via PI3K/AKT signaling in breast cancer. *Adv. Sci.*, **2023**, *10,* 2204819.

[26] Herrera-Abreu, M. T.; Palafox, M.; Asghar, U.; Rivas, M. A.; Cutts, R. J.; Garcia-Murillas, I.; Pearson, A.; Guzman, M.; Rodriguez, O.; Grueso, J.; et al. Early adaptation and acquired resistance to CDK4/6 inhibition in estrogen receptor-positive breast cancer. *Cancer Res.* **2016**, *76* ,2301–2313.

[27] Seiwert, T. Y.; Zuo, Z.; Keck, M. K.; Khattri, A.; Pedamallu, C. S.; Stricker, T.; Brown, C.; Pugh, T. J.; Stojanov, P.; Cho, J.; et al. Integrative and comparative genomic analysis of HPV-positive and HPV-negative head and neck squamous cell carcinomas. *Clin. Cancer Res.* **2015**, *21*, 632–641.

[28] Zhang, Y.; Wei, G.; Liu, W.; Li, T.; Wang, Y.; Zhou, M.; Liu, Y.; Wang, X.; Wei, H. Nanozymes for nanohealthcare.

[29] Wei, H.; Wang, E. Nanomaterials with enzyme-like characteristics (nanozymes): Next-generation artificial enzymes. *Chem. Soc. Rev.* **2013**, *42*, 6060–6093.

[30] Meng, X.; Zhu, G.; Sun, S.; Yao, W.; Zhang, Y.; Yang, Y.-G.; Sun, T. Nanozymes for Liver Disease Therapy: Advances in catalytic activity, targeting strategies, and clinical translation. *Adv. Sci. 13*, e74590.

[31] Zhao, Y.-Y.; Lu, L.; Jeong, H.; Kim, H.; Li, X.; Zhang, H.; Yoon, J. Enhancing biosafety in photodynamic therapy: progress and perspectives. *Chem. Soc. Rev.* **2025**, *54*, 7749–7768.

[32] Zhang, Y.; Zhang, Y.; Liang, R.; Zou, J.; Pei, R.; Chen, X. Targeted ROS scavenging for disease therapies using nanomaterials. *Adv. Mater.* **2025**, *37*, e04435.

[33] Soe, S. K.; Ullah, Z.; Roy, S.; Madni, M.; Yan, Y.; Chen, D.; Maridevaru, M. C.; Zhang, Y.; Kyaw, A. K. K.; Zhang, S.; et al. A new insight into balancing reactive oxygen species in piezodynamic therapy. *Adv. Funct. Mater.* **2026**, *36*, e13106.

[34] Li, H.; Wang, N.; Mao, X. Incidental vs. engineered nanoparticles in Alzheimer's and Parkinson's disease: Pathological pathways and therapeutic interventions. *Nano Res.* **2025**, *18*, 94908055.

[35] Cui, Y.; Wang, R.; Qin, J.; Wang, X. Nanozyme-driven closed-loop regulation of antitumor immunity: From catalytic reprogramming to immunological synergy. *Nano Res.* **2025**, *18*, 94907967.

[36] Zhang, R.; Jiang, B.; Fan, K.; Gao, L.; Yan, X. Designing nanozymes for in vivo applications. *Nat. Rev. Bioeng.* **2024**, *2*, 849–868.

[37] Li, Z.; Ding, B.; Li, J.; Chen, H.; Zhang, J.; Tan, J.; Ma, X.; Han, D.; Ma, P.; Lin, J. Multi-enzyme mimetic MoCu dual-atom nanozyme triggering oxidative stress cascade amplification for high-efficiency synergistic cancer therapy. *Angew. Chem. Int. Ed.* **2024**, *64*, e202413661.

[38] Tang, C.; Chao, X.; Feng, W.; Dai, X.; Chen, Y.; Zhang, S. Machine learning-assisted screening of high-entropy Sub-1 Nm nanowires for ultrasound-augmented pancatalytic tumor therapy. *J. Am. Chem. Soc.* **2026**, *148*, 7251–7266.

[39] Zhang, Y.; Yang, S.; Xiang, Q.; Huang, J.; Tan, Y.; Peng, X.; Feng, Y.; Chang, R.; Li, J.; Cheng, Y.; et al. Atomic-precision triple-enzyme nanozyme synchronizes mitochondrial dual-pathway disruption for precision oncology. *Angew. Chem. Int. Ed.* **2026**, *65*, e20859.

[40] Wang, Q.; Liu, S.; Li, C.; Huang, Y.; An, B.; Wang, M.; Qu, J.; Wang, P.; Xu, J.; Ma, P. Fe-O-Mo site-activated nanozymes for bienzymatic/upconversion synergistic catalytic anticancer therapy. *Angew. Chem. Int. Ed.* **2025**, *64,* e202511471.

[41] Han, J.; Jia, E.; Gao, Y.; Liu, B.; Fan, K.; Luo, M. Design of a CuFe tetal–organic framework nanozyme to enhance radiotherapy efficacy via mitochondrial oxidative stress amplification and induction of ferroptosis and cuproptosis. *Nano Res.* **2025**, *18*, 94908023.

[42] Chong, Q.-Y.; Kok, Z.-H.; Bui, N.-L.-C.; Xiang, X.; Wong, A. L.-A.; Yong, W.-P.; Sethi, G.; Lobie, P. E.; Wang, L.; Goh, B.-C. A unique CDK4/6 inhibitor: current and future therapeutic strategies of abemaciclib. *Pharmacol. Res.* **2020**, *156*, 104686.

[43] Rubin, S. M.; Sage, J.; Skotheim, J. M. Emerging strategies to inhibit the G1/S transition for cancer therapy.

Cancer Res. **2026,** *86*, 1545–1557.

[44] Yang, Y.; Luo, J.; Chen, X.; Yang, Z.; Mei, X.; Ma, J.; Zhang, Z.; Guo, X.; Yu, X. CDK4/6 Inhibitors: A novel strategy for tumor radiosensitization. *J. Exp. Clin. Cancer Res.* **2020**, *39*, 188.

[45] Wang, Z.; Wang, X.; Dai, X.; Xu, T.; Qian, X.; Chang, M.; Chen, Y. 2D catalytic nanozyme enables cascade enzyodynamic effect-boosted and Ca^{2+} overload-induced synergistic ferroptosis/apoptosis in tumor. *Adv. Mater.* **2024,** *36***,** 2312316.

Electronic Supplementary Material

A multi-enzyme mimetic nanozyme sensitizes esophageal cancer to CDK4/6 inhibition via oxidative stress

Ling Lan[1,2,§], Jiwen Fan[3,§], Yang Li[4,§], Zihan Li[3], Zhu Yuan[1], Imran Shakir[5], Binwu Ying[3], Limei Luo[3](✉), Yi Li[3](✉), Xuping Sun[6,7], and Jin Zhou[2](✉)

[1] *Department of Biotherapy, Cancer Center and State Key Laboratory of Biotherapy, West China Hospital, Sichuan University, Chengdu 610041, China*
[2] *Division of Liver Surgery, Department of General Surgery, West China Hospital, Sichuan University, Chengdu 610041, China*
[3] *Department of Laboratory Medicine/Clinical Laboratory Medicine Research Center, West China Hospital, Sichuan University, Chengdu 610041, China*
[4] *Division of Gastrointestinal Surgery Ward, Department of General Surgery, West China Hospital, Sichuan University, Chengdu 610041, China*
[5] *Department of Physics, Faculty of Science, Islamic University of Madinah, Madinah 42351, Saudi Arabia*
[6] *Center for High Altitude Medicine, West China Hospital, Sichuan University, Chengdu 610041, China*
[7] *College of Chemistry, Chemical Engineering and Materials Science, Shandong Normal University, Jinan 250014, China*
[§] *Ling Lan, Jiwen Fan, and Yang Li contributed equally to this work.*

Supporting information to https://doi.org/10.26599/NR.2026.94908832

Materials: Sodium nitrate ($NaNO_3$), sodium acetate (NaAc), glutathione (GSH), Rhodamine B, 3,3′,5,5′-tetramethylbenzidine (TMB), potassium chloroplatinate (K_2PtCl_6), and 5,5-dimethyl-1-pyrroline N-oxide (DMPO) were purchased from Aladdin (Shanghai, China) were purchased from Aladdin Co., Ltd. (Shanghai, China). DSPE-PEG-OH (MW 2000), and 4′,6-diamidino-2-phenylindole (DAPI) were also obtained from Aladdin. Formamide, hydrogen peroxide (H_2O_2), and glacial acetic acid were supplied by Beijing Chemical Reagents Company. Biological reagents including fetal bovine serum (FBS), 2′,7′-dichlorofluorescin diacetate (DCFH-DA), Cell Counting Kit-8 (CCK-8), Annexin V-FITC/PI apoptosis kit, JC-1 mitochondrial membrane potential kit, and ATP detection kit were purchased from Beyotime Biotechnology (China). All reagents used in this work were analytical grade without further purification.

Characterizations: The crystalline structures of the synthesized materials were analyzed using X-ray diffraction (XRD) on a Bruker D8 Advance diffractometer. Surface morphology and microstructure were examined by scanning electron microscopy (SEM, ZEISS Gemini SEM 300) and transmission electron microscopy (TEM, JEOL JEM-F200). Elemental distribution and atomic-level structural information were obtained using high-angle annular dark-field scanning transmission electron microscopy (HAADF-STEM) equipped with energy-dispersive X-ray spectroscopy (EDX) mapping on a Thermo Scientific Titan 80-300 microscope operating at 300 kV. Surface chemical compositions were determined by X-ray photoelectron spectroscopy (XPS) using a Thermo Scientific Nexsa G2 system with Al Kα radiation. Optical absorption spectra were recorded on a Shimadzu UV-2700 UV–vis spectrophotometer. Dynamic light scattering (DLS)

and zeta potential measurements were performed with a Malvern Zetasizer Nano instrument. Electron spin resonance (ESR) spectra were recorded using a Bruker EMXnano spectrometer at room temperature. Flow cytometric analyses were conducted on a CytoFlex flow cytometer (Beckman Coulter). Fluorescence imaging was performed using an inverted fluorescence microscope (Leica DMi8).

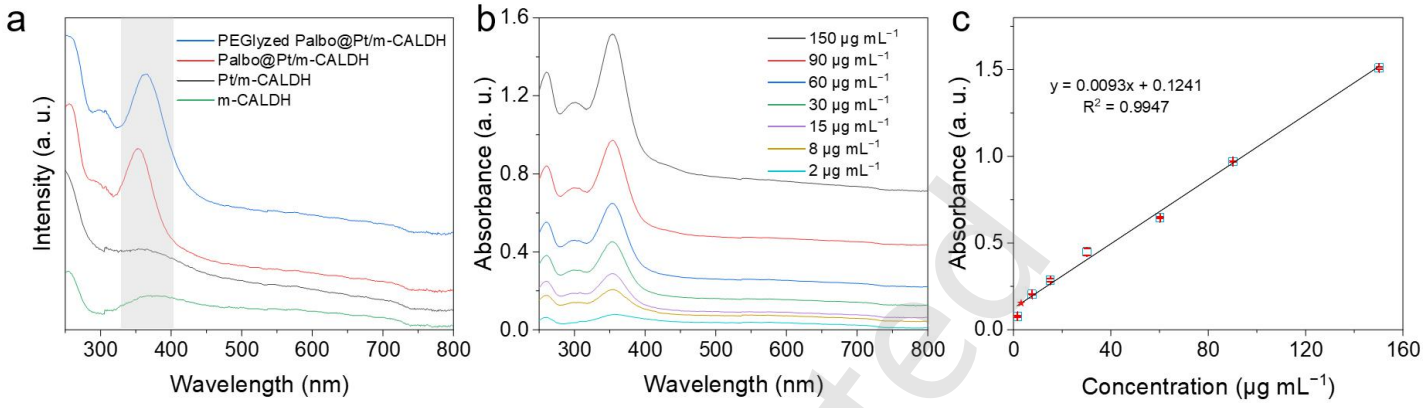

Figure S1 (a) UV-vis spectra of different samples. (b) UV-vis spectra of free palbo at varying concentrations. (c) Linear correlation between absorbance intensity and palbo concentration.

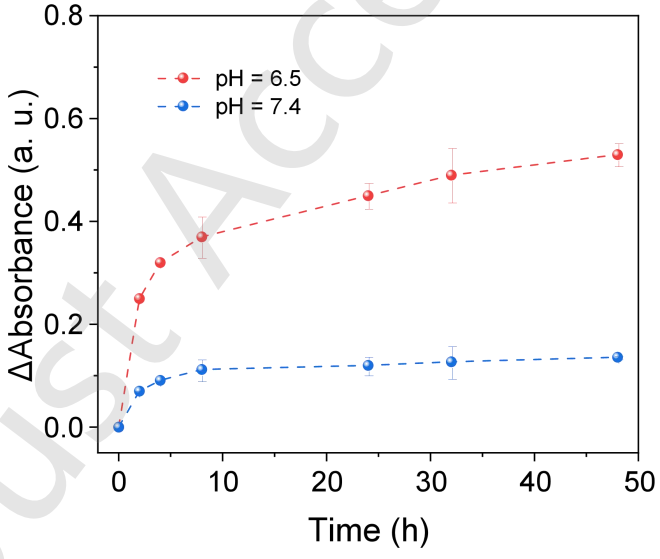

Figure S2 UV–vis absorbance changes during palbo release from Palbo@Pt/m-CALDH under physiological conditions and tumor-mimicking microenvironment.

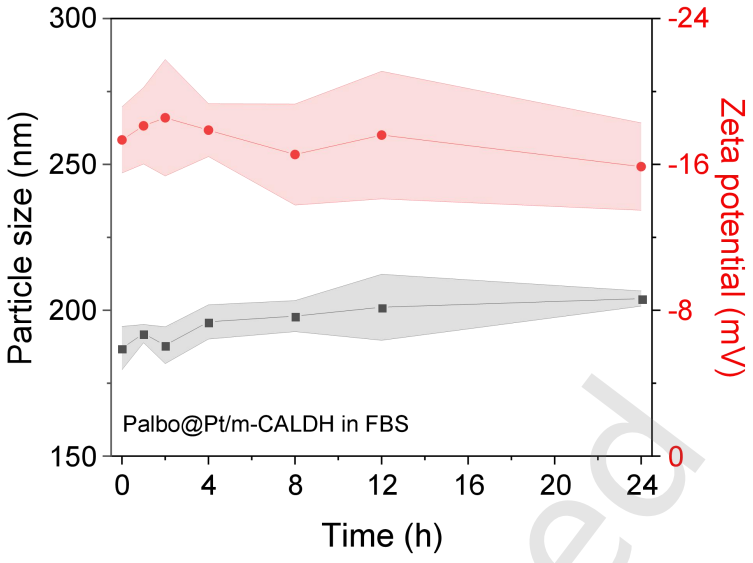

Figure S3 Hydrodynamic diameters and zeta potentials of PEGylated Palbo@Pt/m-CALDH in FBS.

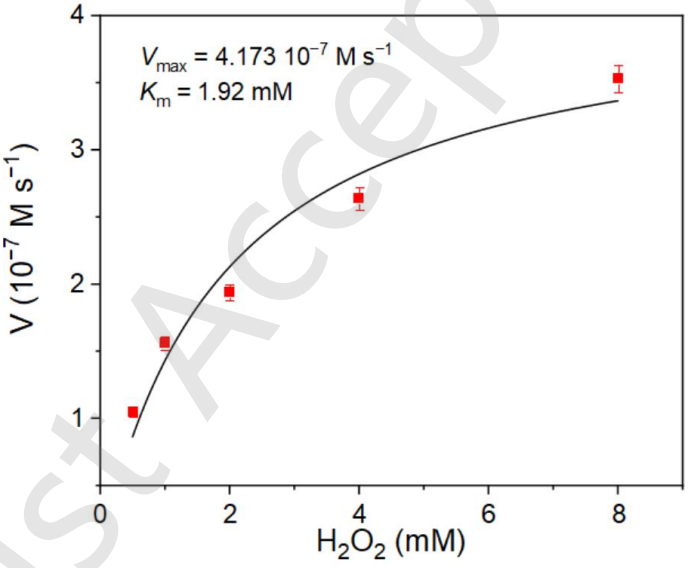

Figure S4 Steady-state kinetics of Palbo@Pt/m-CALDH for H_2O_2.

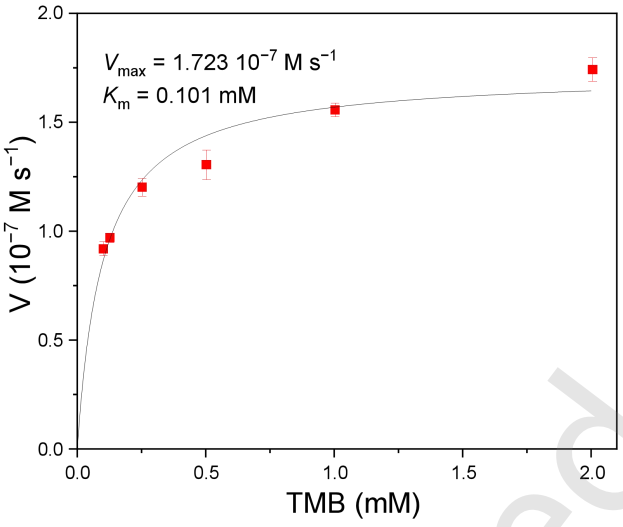

Figure S5 Steady-state kinetics of Palbo@Pt/m-CALDH for TMB in the presence of H_2O_2.

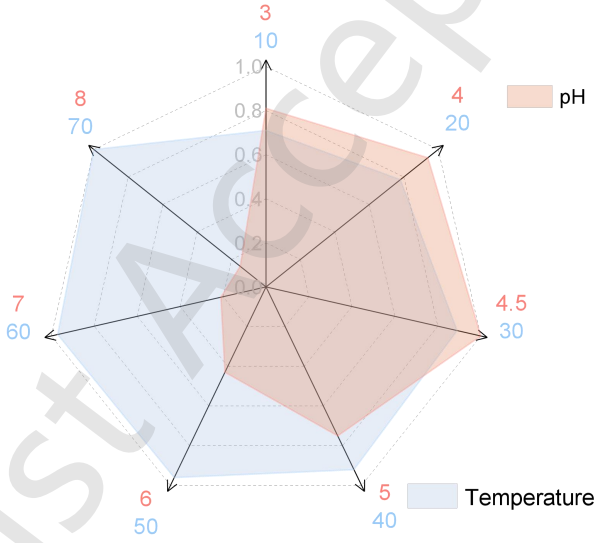

Figure S6 POD-like activity of Palbo@Pt/m-CALDH under different pH values and temperatures.

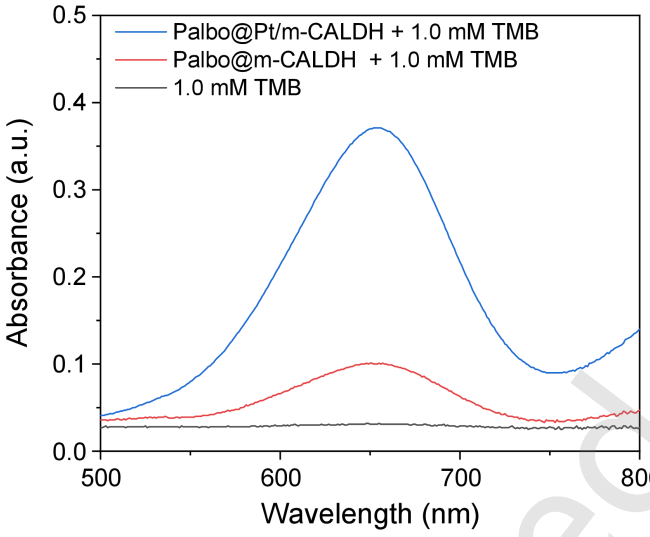

Figure S7 UV–vis spectra of oxTMB in different groups.

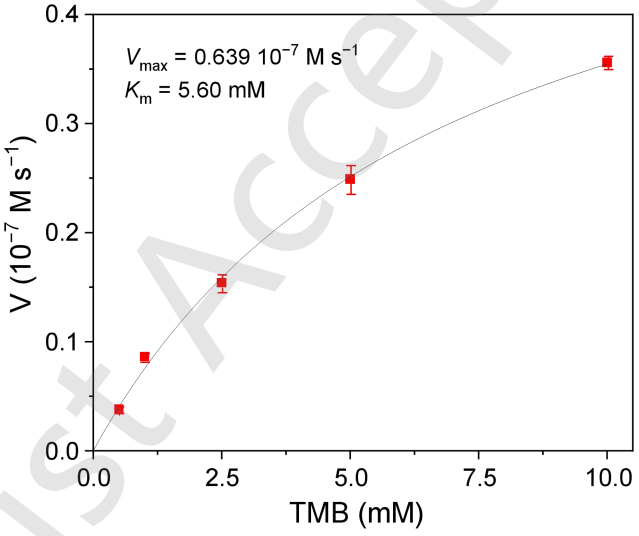

Figure S8 Steady-state kinetics of Palbo@Pt/m-CALDH for TMB.

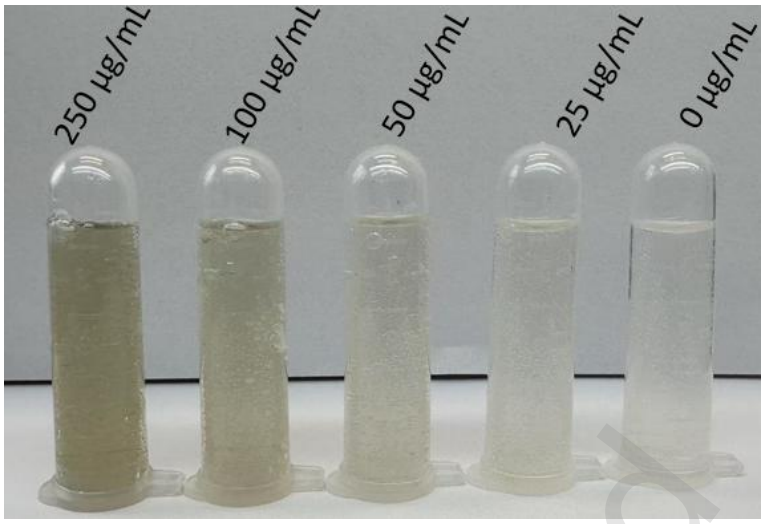

Figure S9 Digital photo of different concentration Palbo@Pt/m-CALDH in the presence of H_2O_2.

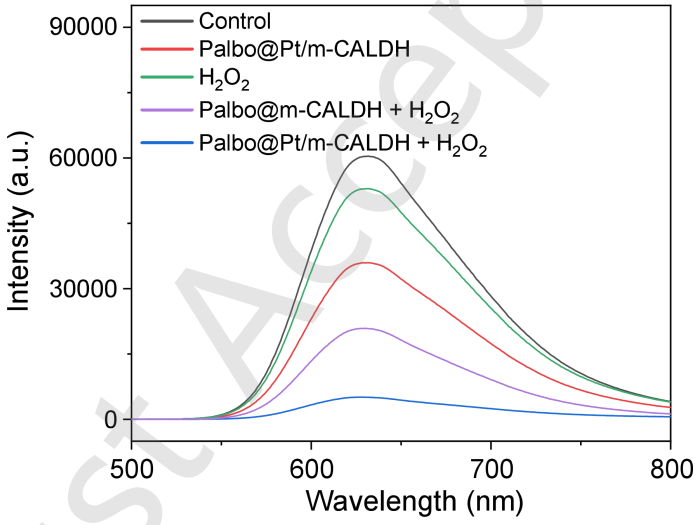

Figure S10 Fluorescence spectra of oxygen sensor in different groups.

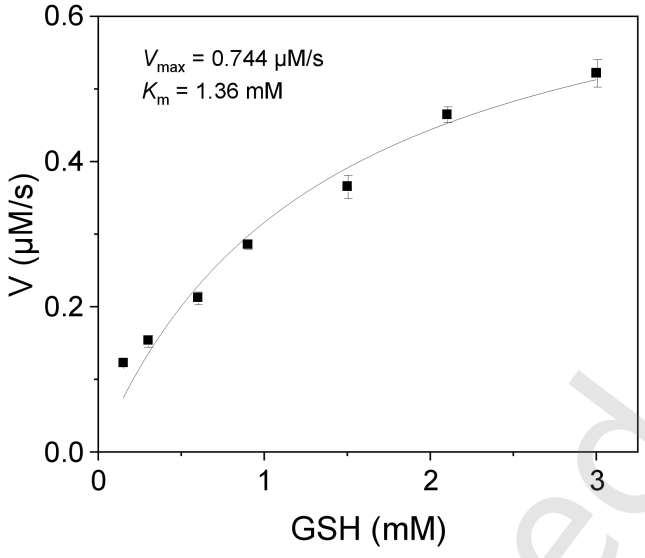

Figure S11 Steady-state kinetics of Palbo@Pt/m-CALDH for GSH.

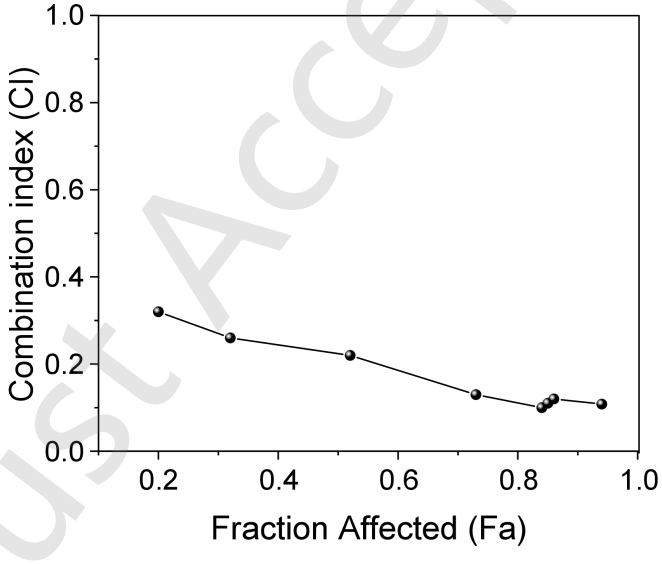

Figure S12 CI analysis for evaluating the synergistic effect between palbo and Pt/m-CALDH. CI values were calculated using CompuSyn software, where CI = 1 indicates an additive effect, CI > 1 indicates antagonism, and CI < 1 indicates synergy.

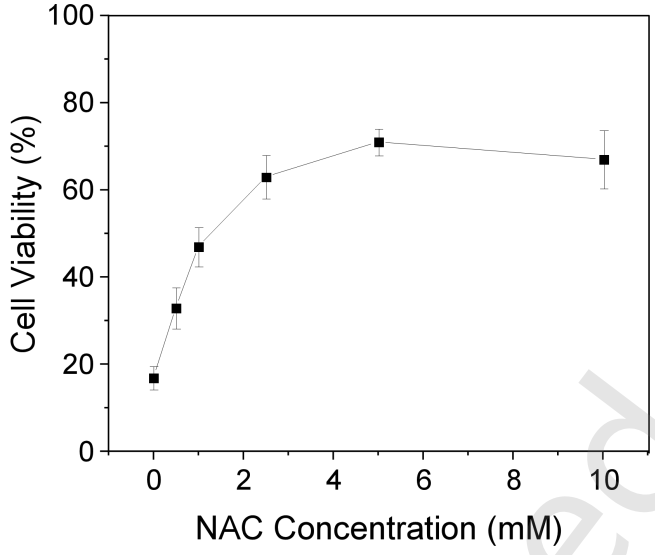

Figure S13 CCK-8 assays of Palbo@Pt/m-CALDH treatment to AKR in the presence of NAC.

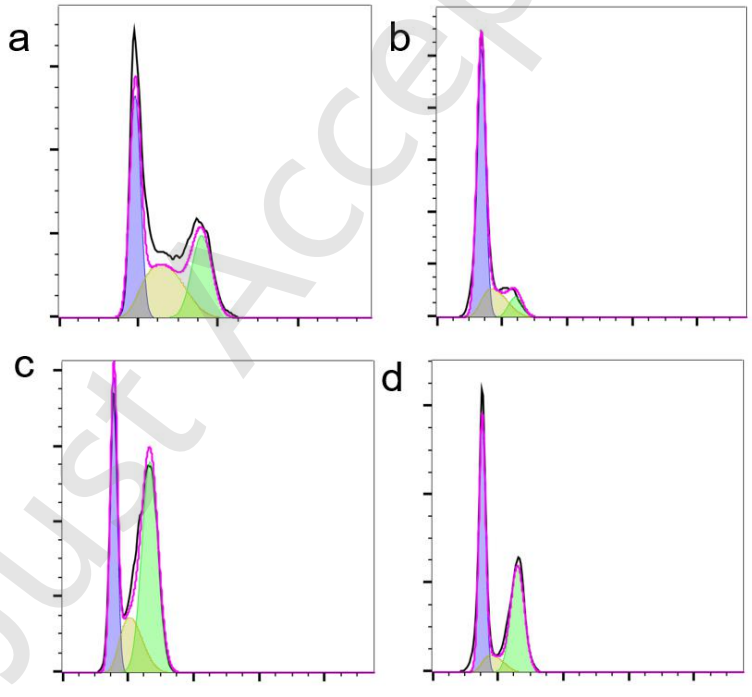

Figure S14 Flow cytometric quantification of cell-cycle distribution under different treatments. Groups: a Control, b Palbo, c Pt/m-CALDH, and d Palbo@Pt/m-CALDH.

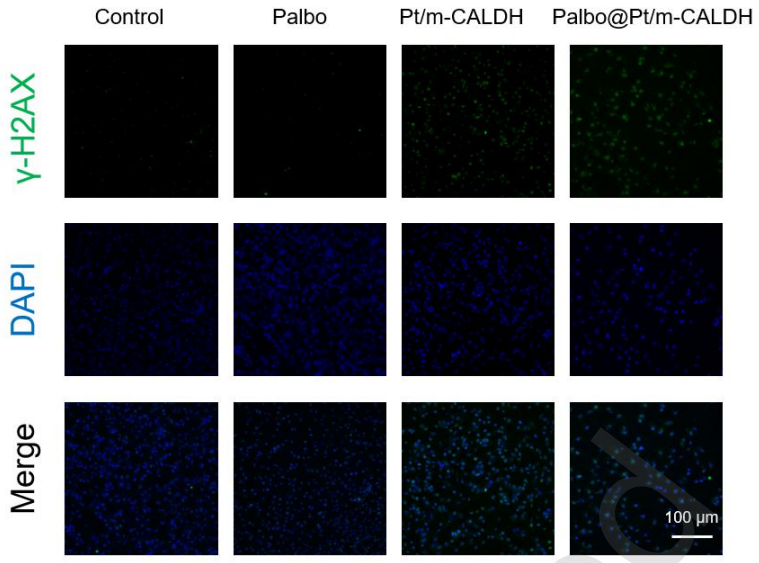

Figure S15 DNA damage analysis using γ-H2AX staining.

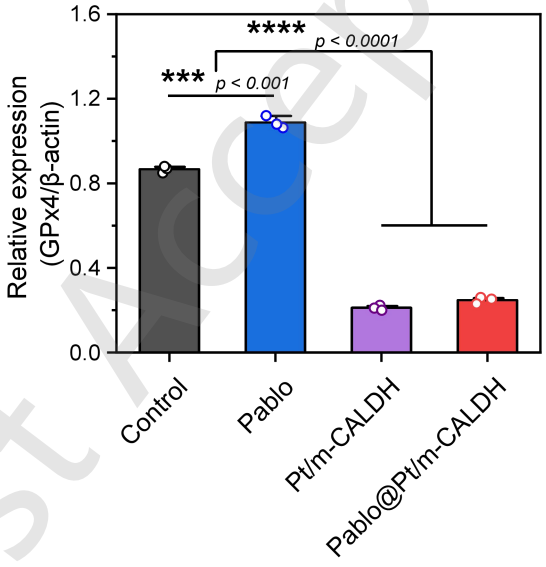

Figure S16 GPX4 corresponding quantitative analysis.

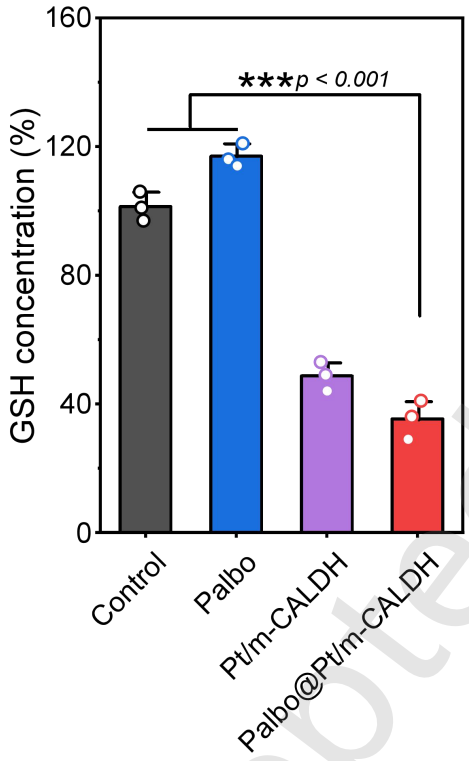

Figure S17 GSH levels in different groups using GSH assay kit (Beyotime, S0053).

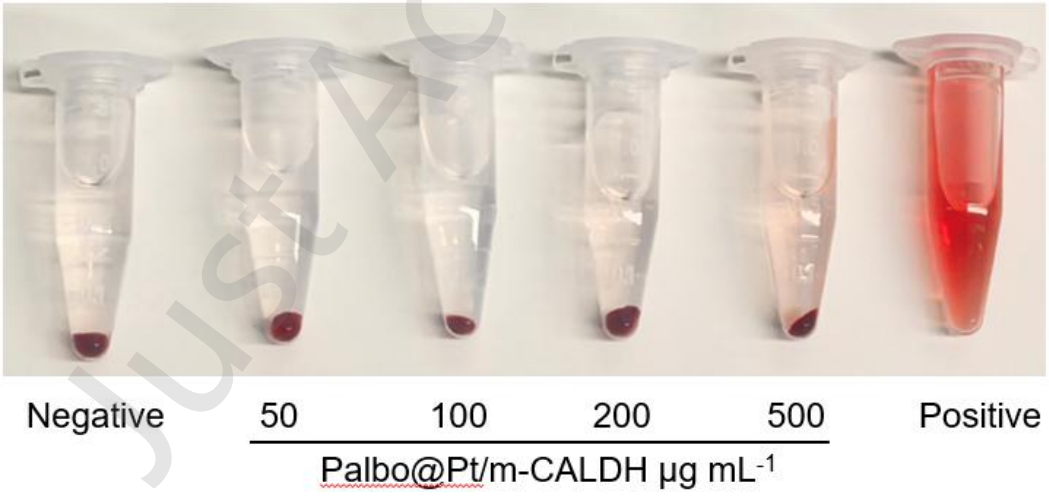

Figure S18 Hemolysis assay results for Palbo@Pt/m-CALDH at various concentrations.

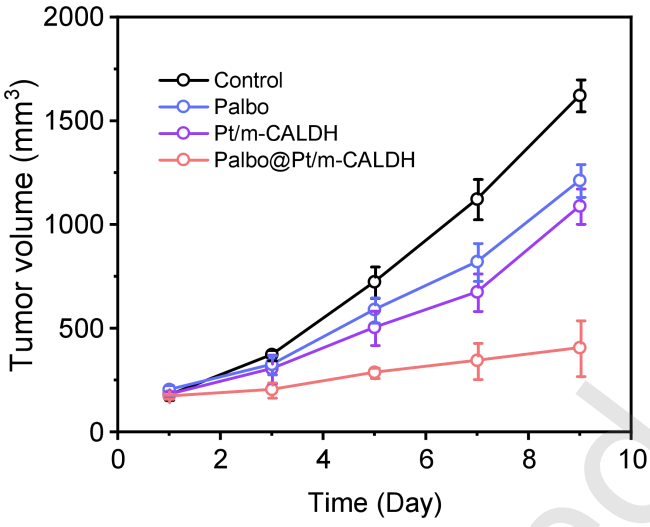

Figure S19 Tumor growth curves of different treatment groups over time.

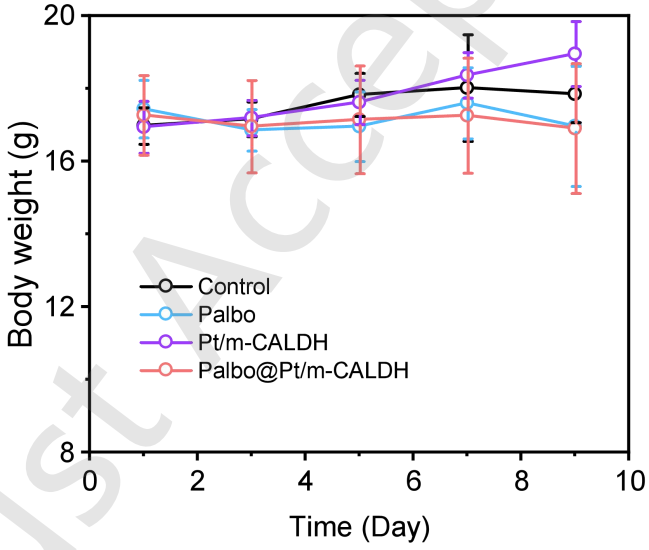

Figure S20 Body weight change curves of different treatment groups over time.

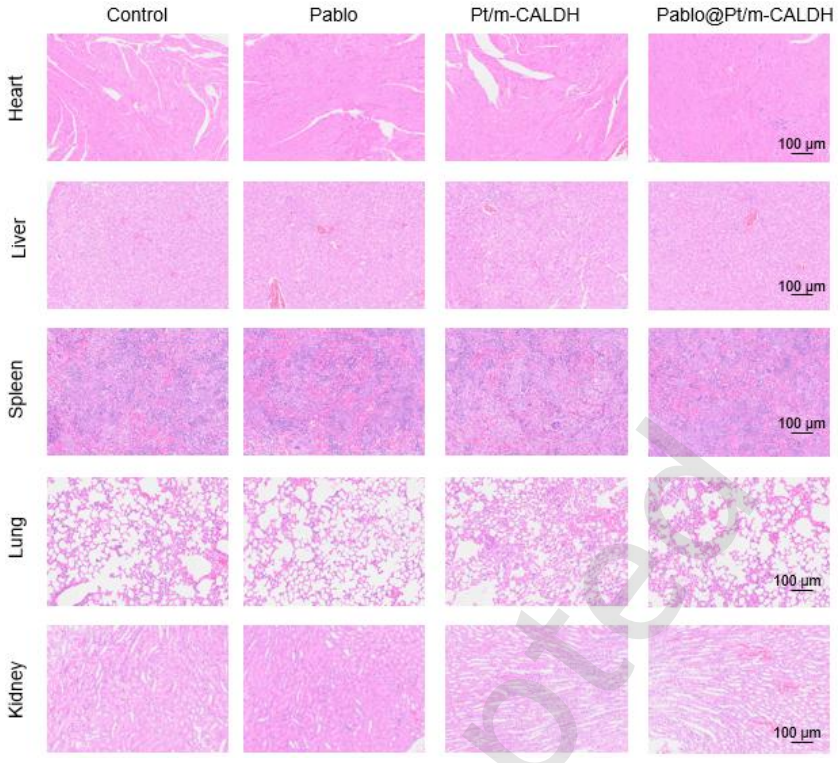

Figure S21 HE staining of major organs after various treatments.

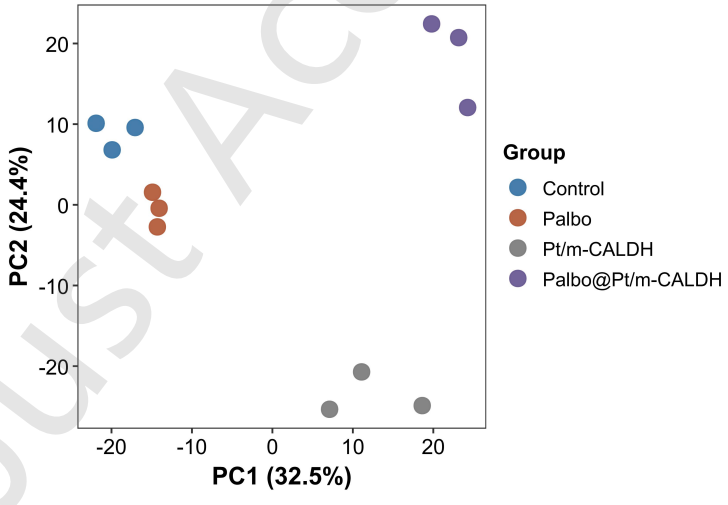

Figure S22 PCA analysis among four groups.

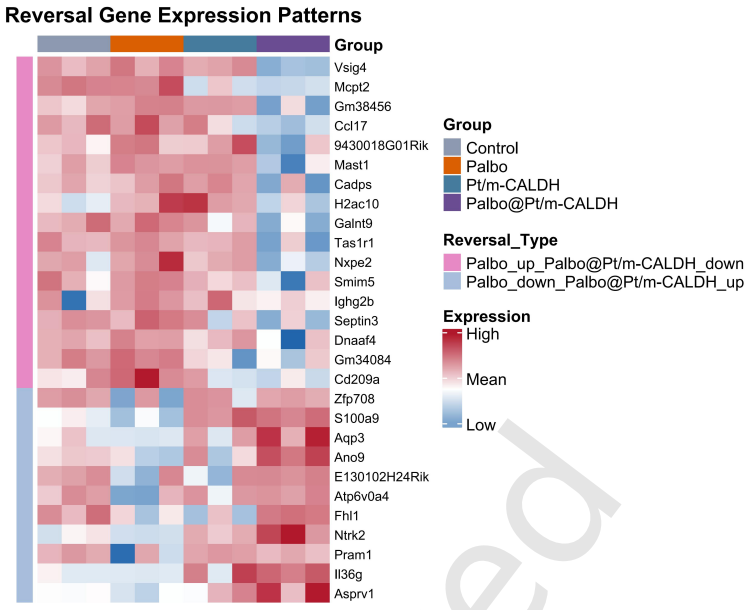

Figure S23 Reversal gene expression analysis heap map among different groups.

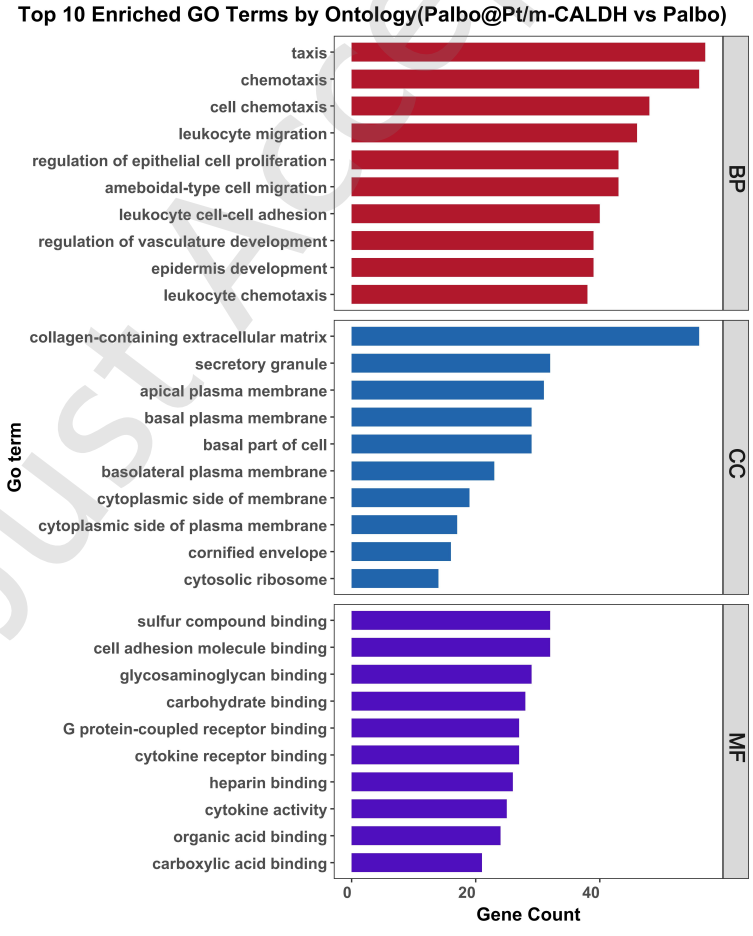

Figure S24 GO enrichment analysis of DEGs in Palbo@Pt/m-CALDH -treated groups